Cite this article as: Galen I., et al. (2026). Translational Changes upon Aging and Dietary Restriction in Progeroid DNA-Repair-Deficient Mice, *AgingBio*, *4*, e20260043. doi: 10.59368/agingbio.20260043.

Research Paper

Translational Changes upon Aging and Dietary Restriction in Progeroid DNA-Repair-Deficient Mice

Ivar van Galen,[1,2] Rutger A. Ozinga,[1,2] Damon A. Hofman,[1,2] Jip van Dinter,[1,2] Sem A. G. Engels,[1] Kimberly Smit,[1,2] Sebastiaan van Heesch,[1,2] Jan H. J. Hoeijmakers[1,2,3,4] and Wilbert P. Vermeij[1,2,*]

[1]Princess Máxima Center for Pediatric Oncology, Utrecht, The Netherlands
[2]Oncode Institute, Utrecht, The Netherlands
[3]Department of Molecular Genetics, Erasmus MC Cancer Institute, Erasmus University Medical Center Rotterdam, Rotterdam, The Netherlands
[4]Institute for Genome Stability in Ageing and Disease, Cologne Excellence Cluster for Cellular Stress Responses in Aging-Associated Diseases (CECAD), University of Cologne, Cologne, Germany
[*]Corresponding author: W.P.Vermeij@prinsesmaximacentrum.nl
https://doi.org/10.59368/agingbio.20260043
Received: 9/5/2025, Revised: 12/19/2025, Accepted: 12/28/2025, Published: 2/3/2026

Aging is a complex multifactorial phenomenon largely driven by damaged macromolecules. We showed recently that with aging, time- and exposure-dependent accumulation of DNA damage derails the basal process of transcription, physically stalling RNA polymerase, lowering and skewing the transcriptional landscape in a gene-length-dependent fashion. However, how this influences the translational output and whether translation is similarly affected is largely unknown. Here, we present a parallel analysis of transcriptional and translational liver profiles from the well-characterized *Ercc1*$^{\Delta/-}$ progeroid, DNA repair-deficient mouse model compared to wild-type under ad libitum conditions and upon dietary restriction (DR), which strongly delays aging in this mutant.

Using ribosome profiling, we found that transcriptional changes during accelerated, normal, and delayed aging are largely preserved at the translational level, ruling out a major translational impact on gene expression in aging. Moreover, in both *Ercc1*$^{\Delta/-}$ and aged wild-type mice there was a prioritization of inflammation, metabolic redesign, and expression of translation initiation factors, along with a shift in codon occupancy. While translation initiation factors were further increased by DR, absolute codon occupancy was partially normalized, showing a discordant response. In addition, increased ribosomal pausing and a relative reduction of upstream open reading frame expression were both further intensified by DR. Together these data infer a fine-tuning of the translational output, for example, by regulating upstream open reading frames under various cellular stress situations. This study uncovers a complex interplay between DR, DNA damage, aging, and translational regulation, highlighting the potential of DR to modify DNA damage-driven translational dynamics during aging.

Introduction

Genomic instability has been posited as a central hallmark of aging and is characterized by the accumulation of a wide range of DNA lesions[1,2]. While most DNA lesions are efficiently resolved by their respective repair systems, some damages escape recognition, are irreparable or repaired incorrectly, leading to the accumulation of mutations and persistent DNA lesions with age[1,3]. This DNA damage drives systemic aging by physically blocking transcription, leading to a lower and particularly imbalanced gene-length-dependent transcriptional output[3–5], and since transcription is essential for every cellular process, this age-related phenomenon of genome-wide transcription stress indirectly affects major aging hallmarks[4,6,7].

Next to a disbalanced transcriptional output, aging does induce a general decoupling between the transcriptome and proteome[8–11]. Furthermore, aging is associated with a dysregulation of proteostasis and a reduction in protein biosynthesis across diverse tissues and organisms[12,13] and can be further altered during age-related diseases[14,15]. Age-driven changes also extend to the stoichiometry of protein complexes, such as the cytosolic ribosome complex, where both a dysregulation between transcript and protein levels and a stoichiometric loss between subunits have been reported[10]. In addition, aging influences translational dynamics, leading to increased ribosome pausing and collisions, shifts in transcript coverage at start and stop codons, and alterations in the translation of upstream open reading frames (uORFs)[16–19], culminating in a reduced and altered translational profile[20]. Interestingly, DNA damage has been implicated in many of the above processes, including derailed transcription[4], inhibited translation[21], and ribosome stalling[22], subsequently contributing to inflammation[23]. However, how DNA damage impacts translation in relation to the before mentioned age-related gene-length-dependent transcriptional imbalance is largely unknown.

To assess the effect of aging and accumulating DNA damage at the level of translation, we compared side-by-side mRNA- and Ribo-seq. For this, we used the well-characterized *Ercc1*$^{\Delta/-}$ DNA-repair-deficient progeroid mouse model[5,24–26]. These mice harbor a single allele coding for a truncated yet partially active ERCC1 variant, a crucial factor involved in multiple DNA repair pathways. The dysfunctional ERCC1 in these mutants leads to a broad variety of unrepaired persisting genomic lesions, accelerating the aging process systemically and limiting their lifespan to 4–6 months[27]. Remarkably, a 30% dietary restriction (DR) regimen, the only evolutionary conserved intervention for extending health and lifespan across multiple species, has been shown to partially mitigate transcriptional aberrations in *Ercc1*$^{\Delta/-}$ mice, prolonging their lifespan up to 200% and strongly delaying the onset of numerous age-related phenotypes[5].

To elucidate if and how transcriptional changes in progeroid *Ercc1*$^{\Delta/-}$ mice are altered at the translational level, we utilized ribosome profiling, a technique that captures a snapshot of active translation. In addition, we investigated how DR, which partially alleviates DNA damage and consequently decelerates aging in these animals, modulates these dynamics, thereby providing insights into the interplay between diet, DNA damage, and translation in the context of DNA damage-driven aging.

Results

Transcription and translation are influenced by genotype and diet

To investigate active translation during DNA-damage-driven accelerated aging and the anti-aging effects of dietary restriction (DR), we selected liver as the primary organ of interest due to its key role in metabolism, detoxification, and the extensively characterized transcriptional landscape during aging in both wild-type (WT) and *Ercc1*$^{\Delta/-}$ progeroid DNA-repair-deficient mice[4,5,28,29]. To capture the progeroid aging phenotype effectively, we focused our analysis on 16-week-old male mice, an age at which *Ercc1*$^{\Delta/-}$ mice exhibit pronounced aging characteristics but prior to becoming overtly moribund[27] and the benefits of DR and weight changes are very prominent[5]. The experimental setup encompassed: *ad libitum* (AL) feeding and 30% DR, maintained over the last ~8 weeks (**Fig. 1A**; **Fig. S1**), which we previously showed to strongly improve health and transcriptional aberrations[5].

Our ribosome profiling data showed a clear 28 nt footprint preference, with about half of all reads considered "clean" as they did not map to tRNA or rRNA sequences (**Fig. 1B,C**). After in-silico removal of tRNA- and rRNA-contaminants, QC revealed >80% of reads mapped to coding sequences (**Fig. S1B**) while showing a strong P-site-specific frame preference indicative of normal tri-nucleotide footprint periodicity (**Fig. 1D,E**). A high-quality mRNA sequencing dataset was generated from the same liver samples to facilitate direct comparison between mRNA- and ribo-seq data (**Fig. S1C**).

Principal Component Analysis (PCA) of both mRNA and ribo-seq data showed distinct clustering and uniformity within and between groups, with primary differentiation based on genotype and diet (**Fig. 1F,G**; **Fig. S1D,E**). Ribo-seq data demonstrated overall somewhat smaller variations among samples from the same group, showing greater homogeneity within and separation between each group compared to the mRNA-seq data. Notably, group distributions for both datasets showed a highly similar arrangement, and the proportional variance of PC1 and PC2 was comparable in both datasets. Thus, these results indicate overall data quality was of high quality and that PCA analysis effectively differentiated the experimental groups, underscoring the distinct characteristics within the data with a highly similar transcriptional and translational output.

ERCC1-deficiency modifies metabolic and inflammatory pathways

When directionality and fold-change differences between *Ercc1*$^{\Delta/-}$_AL and WT_AL at the transcriptional level were compared with those at the translational level, a high degree of concordance was observed (**Fig. 2A**), indicating that globally, translation largely mirrored the transcriptional profile and that translational regulation was limited. Further analysis of the effect of ERCC1-deficiency identified a similar number of significantly differentially transcribed (n = 2429) and translated (n = 2288) genes, with a 45.0% overlap between the two datasets. At both the transcription and translational levels, Ingenuity Pathway Analysis (IPA) revealed in the class of upstream regulators a decrease in PPARA and increases in STAT5B, TNF, TP53, and IFNG (**Fig. 2B,C**), indicative of elevated inflammation/toxicity. Interestingly, when comparing mRNA- and Ribo-seq, the class of immune-related regulators appears more prominent in translation. Immunoglobin, IFN, and Interferon alpha have all strongly moved up in the ranking, and TGF1, which shows a downtrend in transcription, is upward in translation, consistent with the idea of prioritization of immune responses and a capacity for fine-tuning at the level of translation. Metabolic processes were generally downregulated, except for cholesterol biosynthesis and pathways related to its precursors[30], like mevalonate and zymosterol, which in turn were upregulated (**Fig. S2A,B**). These findings were mirrored by the specific upregulation of "LPS/IL-1 mediated inhibition of RXR function," which is associated with impaired lipid metabolism and transport[31,32]. The connection of these pathways to the acute phase response, a response triggered by infection, tissue injury, or inflammation[33,34], was apparent in our context of constitutive DNA damage and further supported by increased p53 signaling (**Fig. 2D,E**). For these processes the ranking in transcription was largely preserved in translation. Importantly, similar concordantly affected pathways and processes were observed when comparing naturally aged 104-week-old WT animals to young 16-week-old controls (**Figs. S1A and S2C–I**).

ERCC1-deficiency alters translational dynamics and open reading frame translation

Natural aging affects various aspects of translation, including fidelity and kinetics[18]. Evaluating the expression of essential components of the translation machinery in *Ercc1*$^{\Delta/-}$_AL mice revealed a significant increase in translation initiation factors (**Fig. 3A**; **Supplemental file 1**), while cytoplasmic and mitochondrial ribosomal subunits were not differentially translated (**Fig. 3B**; **Fig. S3A**). A similar pattern was observed in aged WT_AL mice, which, in addition, did show a significant downregulation of mitochondrial ribosomal subunits (**Fig. S3B–D**).

Next, we examined ribosome pausing, an important aspect of translation kinetics. This process is characterized by a halt or significant slowdown in ribosomal movement along the mRNA strand during protein synthesis and is quantified by the distance and distribution of ribosomal footprints along the mRNA. Analysis of footprint density yielded ribosomal pause site intensity scores and the number of pause sites per gene transcript.

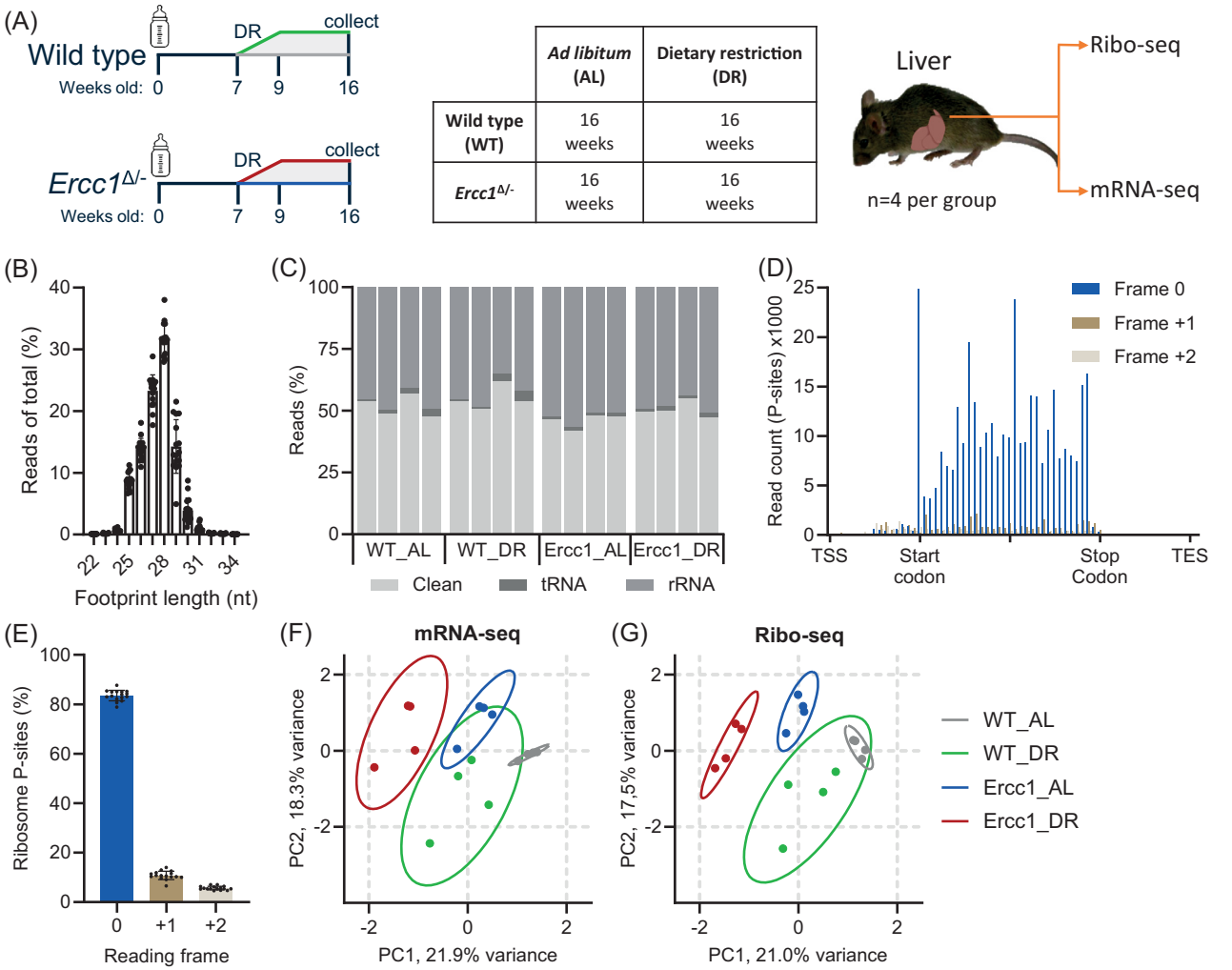

	Ad libitum (AL)	Dietary restriction (DR)
Wild type (WT)	16 weeks	16 weeks
***Ercc1*$^{\Delta/-}$**	16 weeks	16 weeks

Figure 1. Ribosome profiling of *Ercc1*$^{\Delta/-}$ liver results in clear separation between groups. (A) Schematic representation of experimental setup and tissue acquisition from male wild-type and *Ercc1*$^{\Delta/-}$ mice under AL and DR conditions: WT_AL (gray); WT_DR (green); Ercc1_AL (blue); and Ercc1_DR (red). Food was provided to the animals just before the start of the dark (active) period, Zeitgeber Time (ZT) 12:00, except for the day of sacrifice, when no food was given prior to collect between ZT13 and ZT16. **(B)** Footprint length distribution compared to total reads. **(C)** Quantification of RNA contaminants. Reads that were not tRNA or rRNA were considered "clean." **(D)** Gene meta-analysis of p-site-specific frame preference between Transcription Start Site (TSS) and Transcription End Site (TES). **(E)** Quantification of p-site frame preference indicative of footprint periodicity. **(F,G)** PCA plots with 95% confidence intervals for mRNA- **(F)** and Ribo-seq **(G)**. Values are mean ± SD.

Our data showed a significant increase in pause score intensity (Fig. 3C), but no changes in the number of pause sites per gene (Fig. 3D). Neither of these parameters was significantly altered in old WT_AL mice (**Fig. S3F,G**).

To gain further insight into translational dynamics, we assessed codon occupancy, a proxy for the frequency and duration of ribosome binding and translation of specific codons within mRNA sequences[35]. Absolute codon occupancy (pre-normalization for amino acid translational abundance and thus indicative of absolute changes in codon usage between groups) revealed distinct alterations in *Ercc1*$^{\Delta/-}$_AL mice as compared to their wild-type counterparts. Specifically, codons encoding many essential amino acids showed increased occupancy, in addition to nearly all codons for Arginine (R) and Serine (S) (Fig. 3E), but this pattern did not correlate with other amino acid characteristics (**Supplemental file 2**). Interestingly, a strikingly similar change in absolute codon occupancy was observed in old WT_AL animals, including a notable increase in the ACA codon for threonine (T), which exhibited the highest occupancy in both *Ercc1*$^{\Delta/-}$_AL and aged WT_AL mice (**Fig. S3E**). In contrast, relative codon occupancy (normalized for differences in amino acid abundance, which is indicative of altered codon expression within an amino acids' codon family) largely abrogated the earlier observed changes within *Ercc1*$^{\Delta/-}$_AL and old WT_AL animals when compared to young controls (Fig. 3F; **Fig. S3F**). However, some trends, such as for the codons GCU, GGU, ACU, and ACA, remained consistent between relative and absolute codon occupancy.

Next, we examined the translated rates of non-canonical and canonical open reading frames (ORFs) in *Ercc1*$^{\Delta/-}$_AL mice, as these are known to be affected by cellular stressors[36,37]. Upstream ORFs (uORFs), a non-canonical type of reading frame located in the 5' untranslated region (UTR) of mRNAs, have the potential to regulate the translation of downstream canonical coding sequences (CDS). Overlapping uORFs and conventional uORFs tend to inhibit translation of the CDS (Fig. 3G)[36–40]. Relieving this inhibition is part of the cell's adaptive stress response, aiding in homeostatic maintenance and ensuring

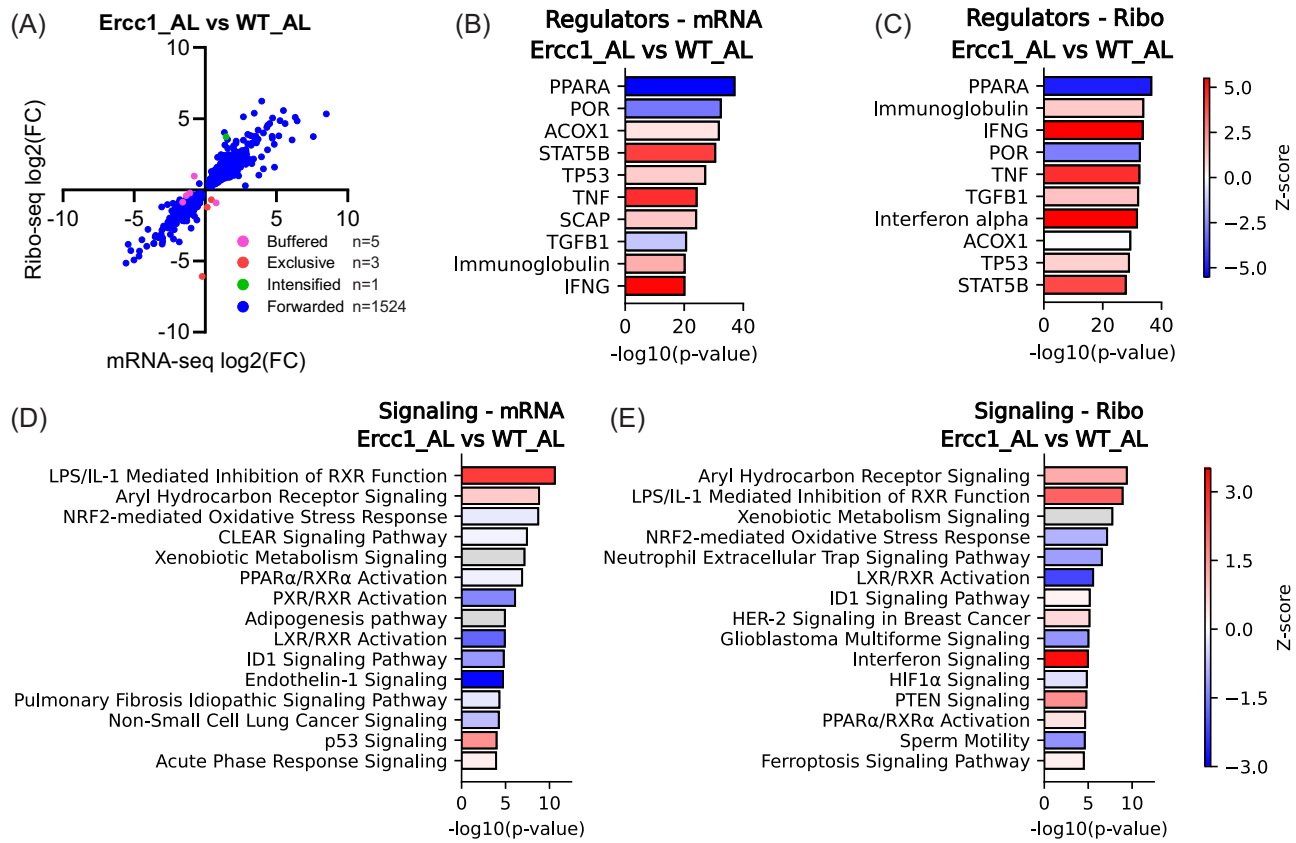

Figure 2. Pathway analysis changes in *Ercc1*$^{\Delta/-}$ mice at the transcriptional and translational level. (A) Scatter plot of gene expression (n = 1533) in *Ercc1*$^{\Delta/-}$ mice, comparing transcriptional (mRNA-seq) and translational (Ribo-seq) levels. Forwarded genes have a significant change in mRNA and ribosome-protected fragments (RPF) at the same rate, with no significant change in translational efficiency (TE). Exclusive genes are regulated only at the translational level, intensified genes have a significant change in TE that acts with the effect of transcription, and buffered genes have a significant change in TE that counteracts the change in RNA. **(B–E)** Upstream regulator **(B,C)** and signaling pathway **(D,E)** analysis based on differentially expressed genes in AL-fed *Ercc1*$^{\Delta/-}$ mice compared to WT at the mRNA **(B,D)** and Ribo-seq **(C,E)** level. Numerical parameters of pathways and upstream regulators were calculated with Ingenuity Pathway Analysis (IPA), and subsidiary pathways were collapsed if top parent pathways were present. Red means upregulated, white indicates pathways with z-scores near zero or those ineligible due to a limited number of hits, blue means downregulated, and gray means that no activity prediction could be made for this pathway.

survival under environmental challenges by enabling enhanced translation of canonical ORFs[41].

In *Ercc1*$^{\Delta/-}$_AL, we identified 101 differentially translated uORF containing transcripts, which were generally downregulated compared to WT_AL (Fig. 3H). Interestingly, a comparative analysis of fold changes between differentially translated uORF and their corresponding canonical CDS revealed that, even though both were downregulated, a markedly stronger translational downregulation happened at the uORF region (Fig. 3I,J; **Fig. S3K**). A similar, albeit less intense, trend was observed in 104-week-old WT_AL mice (**Fig. S3I,J**). In addition, we found a significant overlap between uORFs regulated differentially in accelerated aged *Ercc1*$^{\Delta/-}$_AL and old WT_AL versus young WT controls (Fig. 3K). This overlap showed a set of age-related uORFs whose genes are related to metabolism, cellular stress, and regeneration (**Supplemental file 3A**).

Differences between *Ercc1*$^{\Delta/-}$ and old WT mice

Ercc1$^{\Delta/-}$ mice display an accelerated aging phenotype primarily driven by DNA damage, while natural aging is affected by various stressors, including DNA damage. Comparing directionality and fold-change differences of DEGs at the transcriptional and translational level between 16-week-old *Ercc1*$^{\Delta/-}$ and 104-week-old WT mice showed a high degree of concordance (**Fig. S4A**).

In contrast, IPA upstream regulator analysis showed some disparity between the top mRNA and Ribo results (**Fig. S4B,C**). While the upstream regulators POR and PPARA were both predicted to be decreased in *Ercc1*$^{\Delta/-}$ and old WT when compared to young WT, which has been reported before for natural aging[42]. Direct comparison of *Ercc1*$^{\Delta/-}$ to old WT showed that POR was relatively more inhibited in *Ercc1*$^{\Delta/-}$, while PPARA was increased, potentially due to altered lipid metabolism in *Ercc1*$^{\Delta/-}$ mice[43]. *Ercc1*$^{\Delta/-}$ also showed a markedly lower activity of TGFB1 than old WT, which was more pronounced at the transcriptional level. Notably, NFE2L2 and immunoglobulin complex were predicted to be activated in *Ercc1*$^{\Delta/-}$ mice when compared to old WT, in line with the elevated oxidative stress and altered inflammatory signaling reported for this model (**Fig. S4B,C**)[44].

Analysis of metabolic processes showed that most were relatively increased in *Ercc1*$^{\Delta/-}$ compared to old WT and that they centered around lipid metabolism (as indicated by cholesterol synthesis and fatty acid B-oxidation) and oxidative stress (e.g., increased glutathione-mediated detoxification; **Fig. S4D, E**). In addition, signaling pathways were largely lowered and characterized by LPS/IL-1 mediated inhibition, sirtuin signaling,

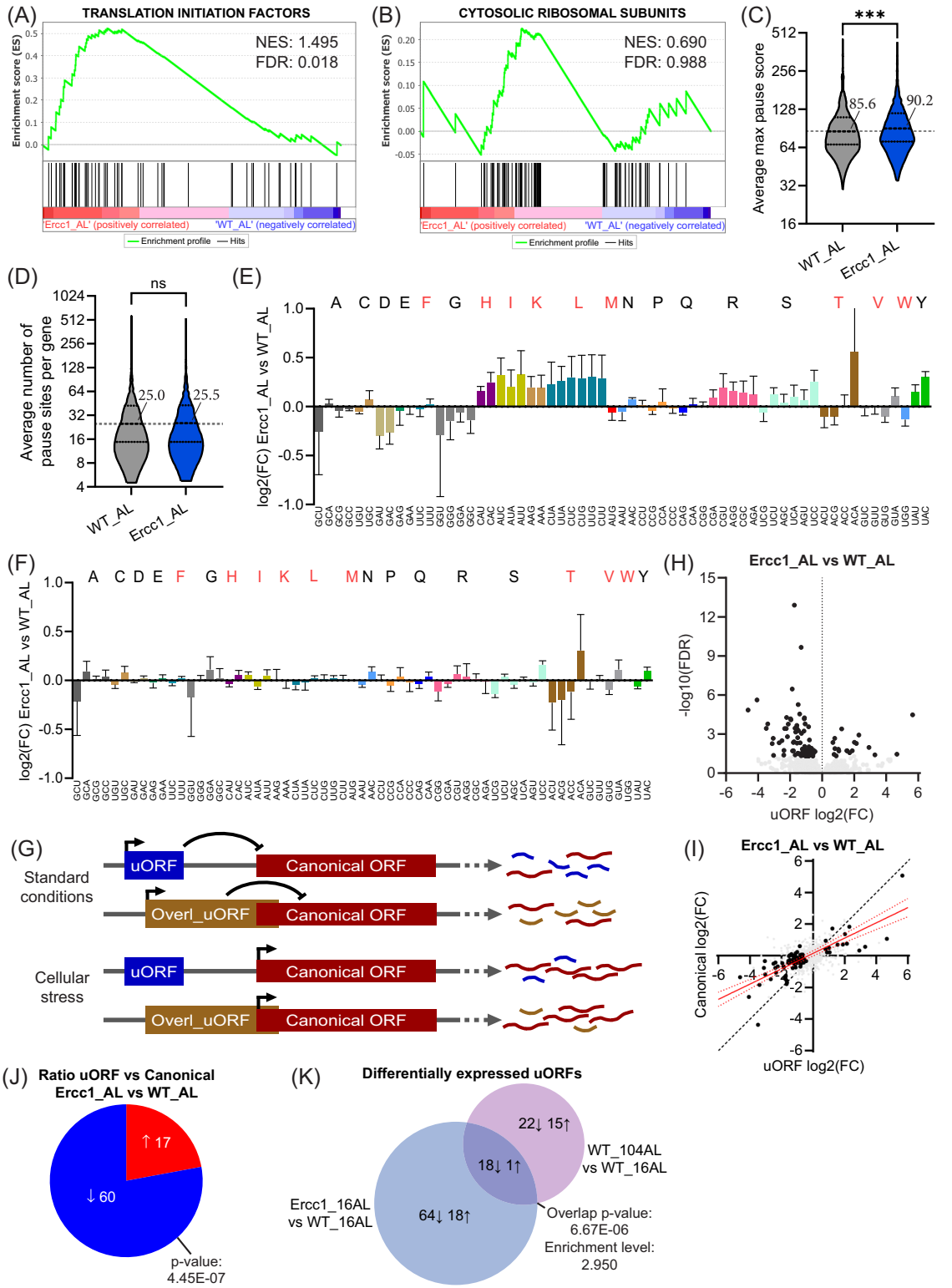

Figure 3. ERCC1-deficiency-driven modifications in translational dynamics and uORF expression. (A,B) GSEA enrichment graphs of translation initiation factors**(A)** and cytosolic ribosomal subunits **(B)**, based on ribosome profiling data **(C,D)** Violin plots depicting the max pause score intensity **(C)** and the mean number of pause sites found per gene transcript averaged per group **(D)**. Highlighted intensity values represent median intensity. **(E,F)** Bar graph plot showing absolute **(E)** and normalized **(F)** P-site codon occupancy log2 fold changes in *Ercc1*$^{\Delta/-}$ as compared to WT with essential amino acids being indicated in red and error bars depicting SD. **(G)** Simplified graphical representation of the regulatory function of (overlapping) upstream open reading frames (uORFs) on a transcript's canonical ORF. **(H)** Vulcano plot of (overlapping) uORF expression in *Ercc1*$^{\Delta/-}$_AL as compared to WT_AL, with differentially regulated uORFs being indicated in black. **(I)** Scatterplot illustrating the relation between uORF and canonical fold change differences in *Ercc1*$^{\Delta/-}$_AL versus WT_AL with significantly altered uORFs being depicted in black. A regression line with a 95% confidence interval, based on the

(legend continued on next page)

significant uORFs, is represented in red. **(J)** Pie chart depicting the number of uORFs that are more strongly up- or down-regulated than the canonical ORF they belong to in *Ercc1*$^{\Delta/-}$_AL as compared to WT_AL. **(K)** Venn diagram of the overlapping differentially regulated uORFs in *Ercc1*$^{\Delta/-}$_AL and 104-week-old WT_AL compared to young 16-week-old WT_AL mice. Arrows indicate activation or inhibition of uORF expression. Significance levels are denoted "ns" for $p > 0.05$ and *** for $p \leq 0.001$, with comparisons made to indicated control groups.

NRF2 oxidative responses (NFE2L2), and NAFLD signaling, all strongly related to stress mechanisms and altered lipid metabolism (**Fig. S4F,G**)[45,46]. As mentioned above, there were differences in absolute codon occupancy in *Ercc1*$^{\Delta/-}$ and old WT that were relatively similar when compared to young WT animals. Direct comparison of *Ercc1*$^{\Delta/-}$ to old WT similarly showed that differences were limited, but that some codon groups (e.g., histidine (H), isoleucine (I), and Tyrosine (Y)) were more highly expressed in *Ercc1*$^{\Delta/-}$ (**Fig. S4H**). Differences in relative codon occupancy were largely negligible, except for AUA, which showed a subtle increase, and AUU and UCG, which decreased in *Ercc1*$^{\Delta/-}$ (**Fig. S4I**). Finally, uORF expression was reduced in *Ercc1*$^{\Delta/-}$ mice, with a more pronounced decrease than observed for canonical ORFs (**Fig. S4J,K**).

DR partially reverses processes affected in *Ercc1*$^{\Delta/-}$ mice

DR alleviates genotoxic stress in *Ercc1*$^{\Delta/-}$ mice, likely by triggering a protective, anti-aging "survival" response boosting maintenance and resilience (e.g., antioxidant defense)[5,47,48]. To evaluate this scenario, we analyzed the expression and translational parameters affected in *Ercc1*$^{\Delta/-}$_DR mice and assessed DNA damage-related changes relative to AL-fed animals. Comparing DR-regulated changes in ribosome profiling data with mRNA again revealed high similarity and equal variance (**Figs. 1F,G** and **4A**; **Fig. S5A–F**). However, the main advantage of Ribo-seq is its ability to examine various aspects of translation and its dynamics; therefore, we primarily focused on this dataset.

The DR-induced differentially expressed genes (DEGs) in *Ercc1*$^{\Delta/-}$ and WT mice showed significant overlap (**Fig. 4B**), with more than 95% altered concordantly (**Fig. 4C**), indicating a highly similar response in both genotypes, consistent with previous findings at the transcript level[5]. However, comparing *Ercc1*$^{\Delta/-}$-induced and DR-driven changes revealed a different pattern: 64% of overlapping genes were regulated discordantly, thus constituting "rescued" *Ercc1*$^{\Delta/-}$ responses by DR, while the 36% concordant DEGs are likely part of the DR-like "survival" response to cellular stresses (**Fig. 4D,E**), which we previously found to be induced in *Ercc1*$^{\Delta/-}$ and other repair mutants[47,49].

Upstream regulator analysis of genes differentially translated in *Ercc1*$^{\Delta/-}$_DR versus AL mutants using IPA revealed an inverse response compared to *Ercc1*$^{\Delta/-}$_AL versus WT_AL mice, in line with DR counteracting the accelerated aging effect in *Ercc1* mutants (**Figs. 2C** and **4F**). These regulators included PPARA, POR, and STAT5B, which are associated with inflammation and lipid metabolism. While pathway analysis of metabolic processes revealed only subtle changes (**Fig. S5G**), signaling processes consistently indicated reduced inflammation and improved liver functioning (**Fig. 4G**). Finally, we found DR to significantly upregulate pathways related to "EIF2 signaling" and the "regulation of eIF4 and p70S6K signaling" in both *Ercc1*$^{\Delta/-}$ and WT genotypes (**Fig. 4G,H**). Both pathways are characterized by the presence of ribosomal subunits, and upregulation of these pathways largely aligns with literature[5,50–52]. Notably, both pathways, essential for the regulation of translation, were not differentially regulated in *Ercc1*$^{\Delta/-}$_AL mice when compared to WT_AL counterparts (**Fig. 2D,E**).

DR differentially regulates translation dynamics in *Ercc1*$^{\Delta/-}$ as compared to WT

We next examined changes to the expression of translation initiation factors and ribosomal subunits in the context of DR in our ribosome profiling data. DR increased the expression of translation initiation factors in both WT and *Ercc1*$^{\Delta/-}$ mice (**Fig. 5A**; **Fig. S6A,B**). The expression of mitochondrial ribosomal subunits was highly variable within each group, but, as mentioned earlier, showed a significant downregulation in WT aging, and DR in *Ercc1*$^{\Delta/-}$ mice significantly reduced subunit levels as compared to DR in WT mice (**Fig. S6C,D**). In contrast, cytosolic ribosomal subunits were significantly upregulated by DR in both genetic backgrounds and significantly lowered in 7- versus 16-week-old *Ercc1*$^{\Delta/-}$ mice (**Fig. 5B**; **Fig. S6E,F**).

Investigating the changes in cytosolic ribosomal subunits, we discerned an atypical expression pattern for *Rpl22l1* as the only significantly increased cytosolic ribosomal subunit protein in *Ercc1*$^{\Delta/-}$ mice when compared to WT (**Fig. 5C**), with an analogous pattern observed in old wild-type animals (**Fig. S6G**). In addition, DR revealed a general upregulation of subunits except for two, *Rps27l* and *Rpl36al*, which were specifically downregulated in *Ercc1*$^{\Delta/-}$ by DR but not in WT mice (**Fig. 5D**; **Fig. S6H,I**). *Rps27l* and its paralog *Rps27* have previously been shown to display an inversely correlated mRNA abundance across various mouse cell types, impacting transcript association[53]. Interestingly, only the combination of DR and the *Ercc1* mutation resulted in the differential expression of these two subunits (**Fig. 5E**).

Continuing our examination of translational dynamics, we found that the number of pause sites per gene showed a homogenous distribution for all groups with no statistical differences (**Fig. 5F**; **Fig. S6J**). On the contrary, DR further enhanced the pause score intensity for *Ercc1*$^{\Delta/-}$ but not in WT mice (**Fig. 5G**; **Fig. S6K**). Finally, DR partially alleviates the absolute non-normalized codon occupancy profile associated with DNA damage and natural aging (**Figs. 3E** and **5H**; **Fig. S7A**). Notably, DR tends to lower the codon occupancy of essential amino acids and some others, such as serine (S) and arginine (R) and the specific ACA codon for threonine (T), potentially reflecting an adaptive response to resource constraints. This DR profile for absolute codon occupancy was significantly less pronounced in WT mice (**Supplemental file 2**). In addition, relative codon occupancy normalized to amino acid abundance revealed that, while overall changes were limited, DR reversed some previously observed trends, including those in GCU, GGU, and threonine codons, between *Ercc1*$^{\Delta/-}$ AL and WT AL mice (**Figs. 3F** and **5I**; **Fig. S7B**). Taken together, the observed changes to the expression of the translational machinery, pause site intensity, and codon occupancy highlight the potential impact of DR on translational dynamics in the context of DNA damage-driven accelerated aging.

DR further downregulates uORF expression in *Ercc1*$^{\Delta/-}$ mice

In addition to the DR-induced changes in translational dynamics, DR drastically increased the number of differentially expressed uORF-containing transcripts in *Ercc1*$^{\Delta/-}$ mice beyond the changes already triggered in AL-fed conditions (**Fig. 6A**). In

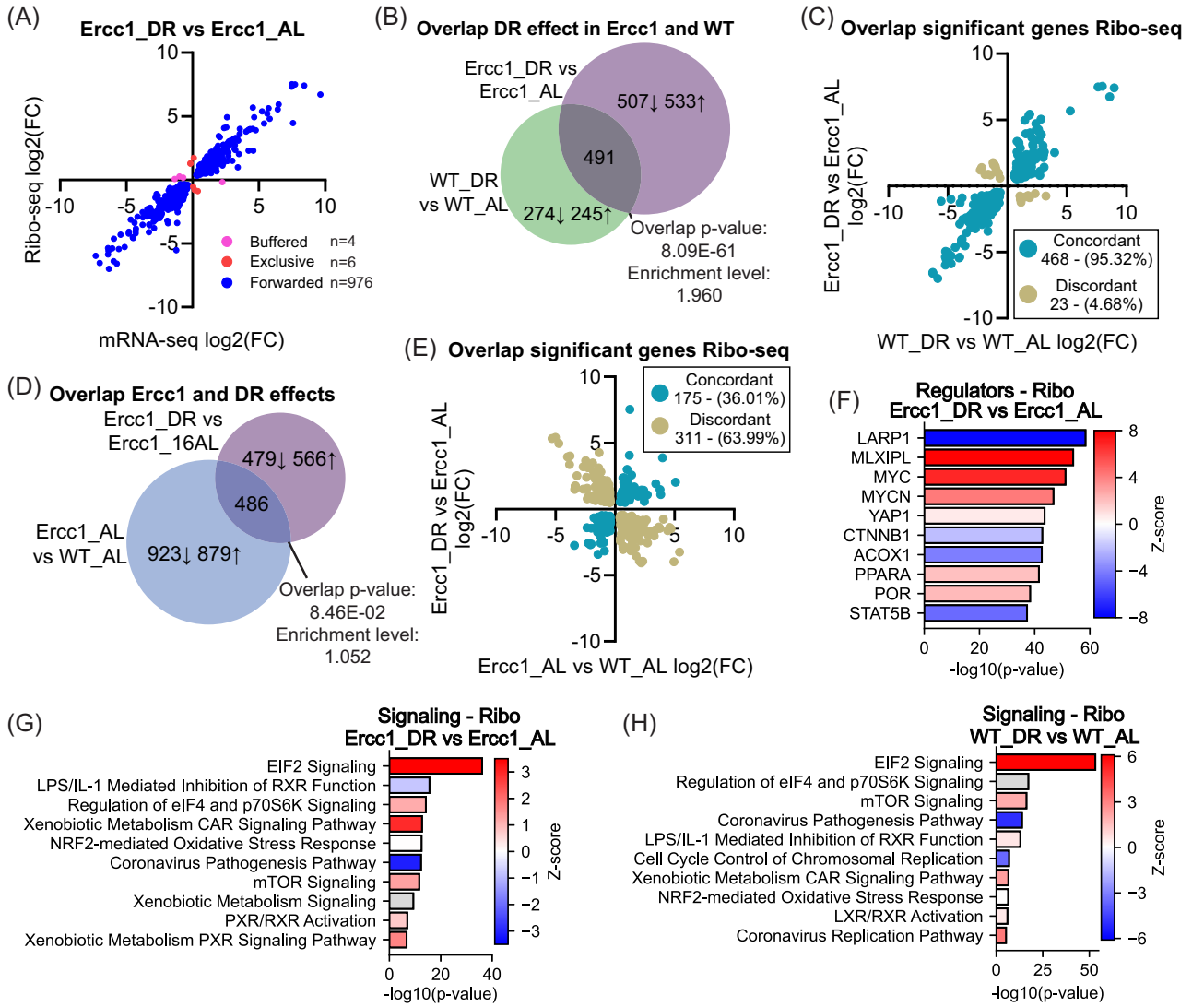

Figure 4. Effect of DR on gene and pathways expression in the liver of *Ercc1*$^{\Delta/-}$ mice. (A) Scatter plot of gene expression (n = 986) in DR-fed versus AL-fed *Ercc1*$^{\Delta/-}$ mice, comparing transcriptional (mRNA-seq) and translational (Ribo-seq) levels. Forwarded genes have a significant change in mRNA and RPF at the same rate, with no significant change in translational efficiency (TE). Exclusive genes are regulated only at the translational level, and buffered genes have a significant change in TE that counteracts the change in RNA. **(B,C)** Venn diagram of the DEGs and their overlap due to DR in *Ercc1*$^{\Delta/-}$ and WT mice as compared to AL-fed controls **(B)**. Scatter plot of the overlapping DEGs divided between concordant and discordant expression **(C)**. **(D,E)** Venn diagram of the DEGs caused by the *Ercc1*$^{\Delta/-}$ mutation, the effect of DR in *Ercc1*$^{\Delta/-}$, and their overlap **(D)**. Scatter plot of the overlapping DEGs divided between concordant and discordant expression **(E)**. **(F)** Upstream regulator analysis of ribosome profiling based on differentially expressed genes in DR versus AL-fed *Ercc1*$^{\Delta/-}$ mice level. **(G,H)** Signaling pathways altered due to DR in *Ercc1*$^{\Delta/-}$ **(G)** and WT **(H)** genotypical background. Numerical parameters of pathways and upstream regulators were calculated with Ingenuity Pathway Analysis (IPA). Red means upregulated, white indicates pathways with z-scores near zero or those ineligible due to a limited number of hits, blue means downregulated, and gray means that an activity prediction could not be calculated for this pathway.

general, DR led to the downregulation of many uORF-containing transcripts in *Ercc1*$^{\Delta/-}$ mice (Fig. 6B; **Fig. S7C**). In contrast, the effect of DR in WT mice was rather limited (**Fig. S7D**), although a significant proportion of differentially expressed uORFs noted in DR-fed *Ercc1*$^{\Delta/-}$ and DR-fed WT overlapped (Fig. 6C; **Supplemental file 3B**). In *Ercc1*$^{\Delta/-}$ mice, but not in WT mice, DR additionally led to the differential inhibition of several uORFs linked to genes related to processes like cellular survival and apoptosis.

As described earlier, the ratio of uORFs to their canonical ORF expression was reduced in *Ercc1*$^{\Delta/-}$ mice. DR further reduced this ratio in *Ercc1*$^{\Delta/-}$ mice, but only marginally in WT mice (Fig. 6D; **Fig. S7E–G**). Quantification of these ratios showed a clear pattern where stress situations reduced the ratio of uORF to canonical ORF expression (Fig. 6E; **Fig. S7H**). This suggests that the interaction between uORF expression and canonical ORF translation is amplified in the context of stress resilience and is particularly evident under conditions of multiple concurrent stressors.

Discussion

Aging induces a variety of changes, including genome-wide transcriptional decline, preferentially affecting long genes, demonstrated first in progeroid DNA repair-deficient *Ercc1*$^{\Delta/-}$ mice and later also with natural aging in numerous species, strengthening the relevance of accelerated aging for understanding normal

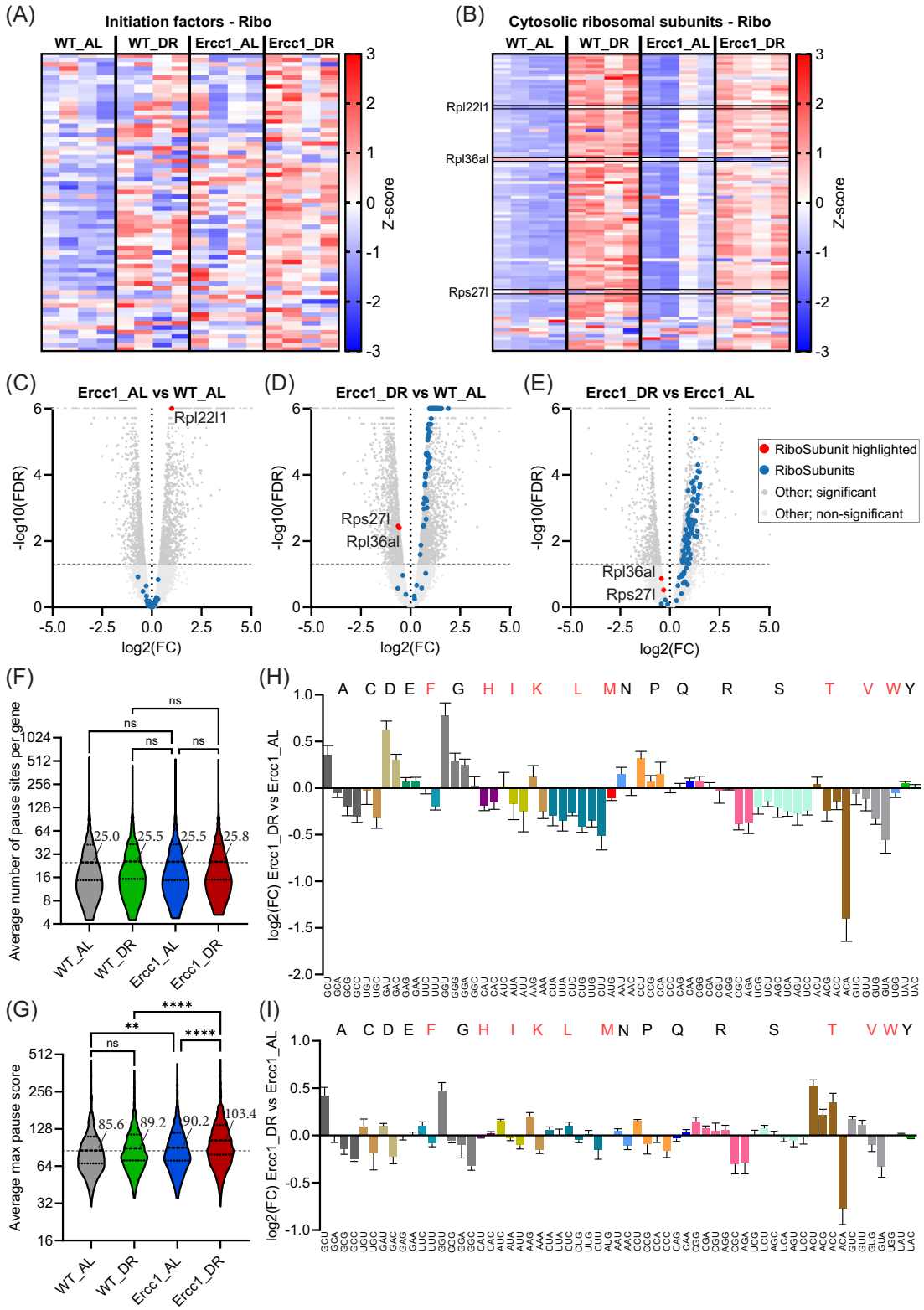

Figure 5. DR modulates translation dynamics in *Ercc1*$^{\Delta/-}$ mice distinctly from WT mice. (A,B) Heatmaps of ribosome profiling expression data for initiation factors **(A)** and cytosolic ribosomal subunits **(B)**, with red indicating an upregulation and blue a downregulation. Relevant factors are highlighted. **(C–E)** Vulcano plots of cytosolic ribosomal subunit expression in ribosome profiling data for the effect of *Ercc1*$^{\Delta/-}$ against WT **(C)**, the effect of DR in *Ercc1*$^{\Delta/-}$ against AL-fed WT mice **(D)**, and the effect of DR in *Ercc1*$^{\Delta/-}$ against AL-fed *Ercc1*$^{\Delta/-}$ **(E)**. Relevant factors are highlighted. **(F,G)** Violin plots displaying the mean number **(F)** and median intensity **(G)** of ribosomal pause site scores averaged per group. **(H,I)** Bar graph plot showing log2 fold changes of absolute **(H)** and aa normalized **(I)** p-site codon occupancy in DR-fed *Ercc1*$^{\Delta/-}$ mice compared to AL-fed *Ercc1*$^{\Delta/-}$. Essential amino acids are indicated in red. Error bars depict SD. Significance levels are denoted "ns" for $p > 0.05$, ** for $p \leq 0.01$, and **** for $p \leq 0.0001$, with comparisons made to indicated control groups.

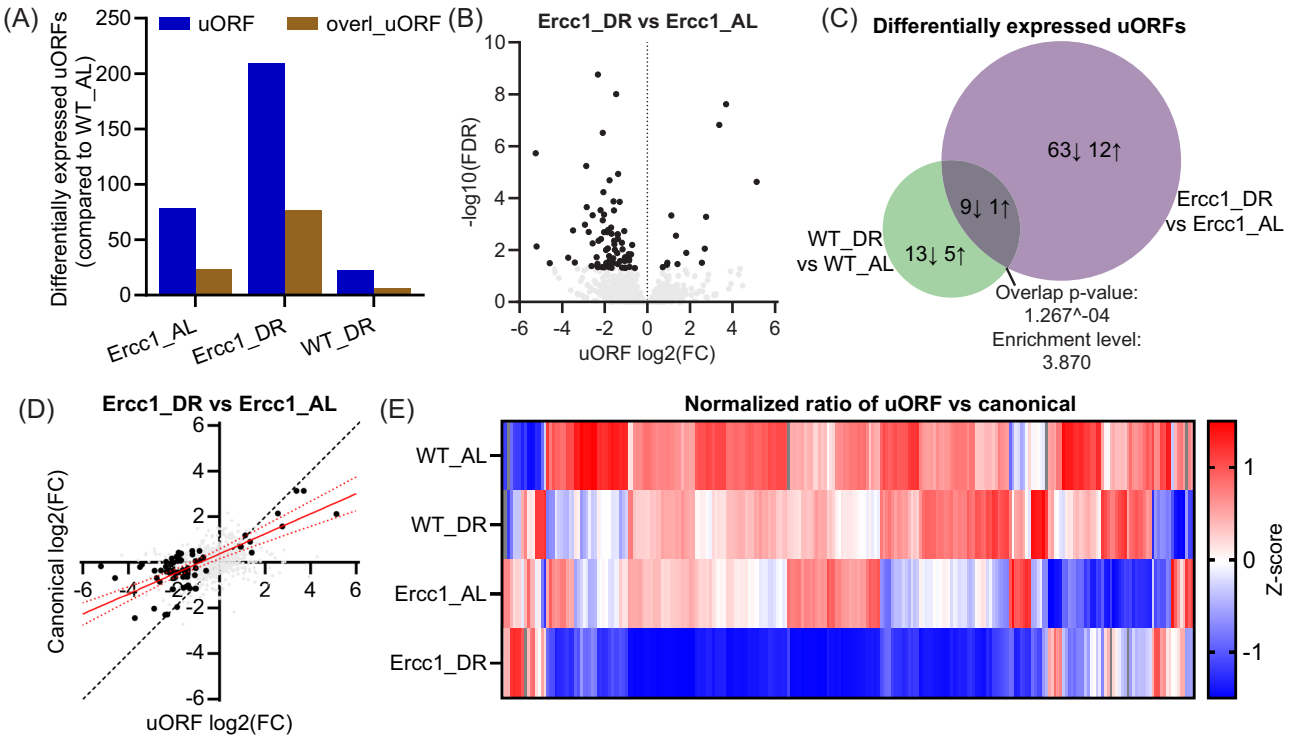

Figure 6. Effects of DR on upstream open reading frames. (A) Bar graph displaying the number of differentially expressed uORFs and overlapping uORFs in *Ercc1*$^{\Delta/-}$ AL or DR-fed and WT DR-fed against WT AL-fed mice. **(B)** Vulcano plot of uORF expression altered by DR in *Ercc1*$^{\Delta/-}$. Black dots are significant, while gray dots are not. **(C)** Venn diagram of differentially expressed uORFs due to DR in WT and *Ercc1*$^{\Delta/-}$ genetic backgrounds. Arrows indicate activation or inhibition of uORF sequence translation. **(D)** Scatterplot illustrating the relation between uORF and canonical fold change differences between DR and AL-fed *Ercc1*$^{\Delta/-}$ mice, with significantly altered uORFs being depicted in black. A regression line with a 95% confidence interval, based on the significant uORFs, is represented in red. **(E)** Heatmap representing the relative ratio between uORF and canonical ORF expression based on all uORFs that were differentially regulated between WT_AL and at least one other group. Red means upregulated, blue means downregulated, and gray means that no direction could be calculated.

aging[4–7,54,55]. Using the liver as a well-characterized organ central to metabolism, we investigated here whether and to what extent these transcriptional changes are counteracted at the translational level or whether translation degenerates as well. Our findings indicate that transcriptional output is largely retained at the translational level in both *Ercc1*$^{\Delta/-}$ and WT mice, regardless of diet or age. In the liver of *Ercc1*$^{\Delta/-}$ mice we observed significant alterations in processes linked to inflammation and metabolism. Many of these responses are stress-related[56,57] and likely triggered by sterile inflammation in response to DNA damage[7,58–60]. Some consequentially altered metabolic pathways could be detrimental. For example, increased AhR signaling activity has been inversely linked to NAD+ metabolism[61,62], while NAD+ supplements have been shown to extend the health and lifespan of mice, including DNA-repair-deficient models[63–67]. Interestingly, many alterations were influenced in an age-related, DNA-damage-dose-dependent manner, while 30% DR ameliorated a variety of tissue-damage-related pathways in *Ercc1*$^{\Delta/-}$ mice, findings that are logically consistent with the anti-aging benefits exerted by DR[5]. Notably, DR influenced translational regulators "eIF2 signaling" and "regulation of elF4 and p70S6K signaling"[50,68,69], which were predominantly enriched for ribosomal subunits. The increased phosphorylation of eukaryotic translation initiation factor elF4 has recently been linked with translation of mRNAs involved in fasting-induced lipid catabolism and ketone body production via a newly discovered lipid-induced AMPK–MNK–eIF4E kinase signaling pathway[50], which aligns with the observed differential regulators and pathway expression in our study.

The distinct expression of certain cytosolic ribosomal subunits under conditions of DNA damage and DR draws attention to potentially unique functions related to translation. Increased expression of *Rpl22l1* during WT and accelerated aging is noteworthy, as it has previously been implicated in processes like proliferation, translation, and epithelial-to-mesenchymal transition[70–72], likely linked to damage-induced cellular turnover. Moreover, DR modified *Rps27l* expression, which has previously been associated with p53 signaling and autophagy[53,73,74]. Concurrently, *Rpl36al* has been postulated to play a role in peptide bond formation and is the only ribosomal protein so far identified that can engage with tRNA, regardless of its ribosomal association[75]. Notably, DR specifically influenced the expression of Rps27l and Rpl36al during conditions of DNA-damage-driven cellular stress but not in young WT, suggesting a synergistic requirement of DNA damage accumulation and nutrient stress.

Curiously, the translation of ribosomal subunits in the liver of naturally aged C57BL/6 mice (32 months) has previously been reported to decrease through inhibition of 5'-TOP-related genes[16]. In contrast, our results demonstrate that DR can increase both the transcription and translation of the translational machinery, while other studies in different animals have reported similar increases at the transcriptional level[10,76]. The reason for this discrepancy is yet unknown but might be related to the improved health in mice with a more outbred-like C57BL6J/FVB hybrid

background as compared to the pure C57BL6J strain. Future work might compare relevant datasets to exclude other aspects such as differences in data handling, normalization, or validate findings more at an absolute quantitative level.

The general upregulation of initiation and cytosolic ribosomal subunits could reflect an attempt to increase ribosomal turnover, enhancing translational regulatory oversight and fidelity, or might be an apparent increase due to the relative nature of sequencing when total transcription and translation decreases. In addition, the absence of changes in mitochondrial ribosomal subunits presents a striking dichotomy, suggesting a disconnect between the regulatory adjustments of cytoplasmic and mitochondrial ribosomal subunits under DR, warranting further examination, also considering the reduced correlation in age-related changes in transcriptome versus proteome[10].

Furthermore, translation dynamics were also influenced, with pause site intensity, absolute codon occupancy, and uORF expression being more strongly affected by ERCC1-deficiency than by WT aging, consistent with known phenotypical differences[27,63]. Moreover, DR in young WT mice showed little effect on various aspects of translational dynamics, while having a strong impact on *Ercc1*$^{\Delta/-}$ mice, further supporting the idea of synergistic interactions in responses between genotoxic- and nutrient-induced cellular stress. Codon occupancy showed a clear discrepancy between the effects caused by the *Ercc1*$^{\Delta/-}$ mutation and DR, with DR reversing the pattern toward AL-fed WT levels. Although correlations with essential amino acid and codon usage were observed, direct mechanistic explanations remain unidentified.

Both relative codon occupancy and ribosomal pausing are linked to ribosomal movement, yet they displayed discordant behavior. However, pause score intensity and relative uORF changes were both concordantly intensified by DR in *Ercc1*$^{\Delta/-}$ mice, suggesting that these processes are potentially beneficial adaptive mechanisms to ensure efficient protein synthesis despite DNA damage and nutrient scarcity. Ribosomal pausing is, for example, an important aspect of translation, affecting protein folding, localization, fidelity, and protein expression by altering the speed of translation elongation[19,77]. However, exacerbation of pausing, that is, ribosomal stalling, during aging has been suggested to disrupt co-translational proteostasis and induce detrimental age-related translational reprogramming, potentially leading to reduced levels of vital proteins and an exacerbation of the aging phenotype in neurological tissues, complicating its mechanistic role[17,22,78]. It remains to be investigated if DNA damage could be an antagonistic pleiotropic regulator, where mild levels of genotoxic stress reduce the speed of translation, while excessive damage drives proteotoxic stress, and whether these effects could be tissue dependent[3,24,79].

A large number of canonical ORFs associated with the uORFs we observed are known to produce proteins crucial for cellular homeostasis. The relative reduction of these uORFs, compared to their canonical counterparts, suggests a protective or adaptive mechanism. Interestingly, uORF-related gene transcripts can also contain other regulatory elements like internal ribosome entry sites (IRES), which are often found in mRNAs coding for master regulators of cellular homeostatic responses. These mRNAs must be tightly controlled, and under various stresses, including DNA damage and amino acid starvation, the relative increased selective translation of these sequences ensures homeostasis[80]. Moreover, while the observed uORF changes are statistically significant, the relatively low number of uORF-related footprints and their potential interaction with IRES elements suggests that further research, potentially involving deeper sequencing, may provide additional insights.

Models of accelerated aging often do not fully encapsulate all aspects of natural physiological aging[3,24,79,81]. However, the *Ercc1*$^{\Delta/-}$ mouse model shows strong similarities with natural aging at both the molecular and physiological level[25,82,83] and similarly displays accelerated glycan- and epigenetic aging clocks across multiple tissues[84–86]. In the current study, differences between accelerated and naturally aged mice were mainly characterized by lipid metabolism. Given the central role of lipid metabolism in longevity, these differences may be partially explained by survival-bias-driven metabolic adaptations in the naturally aged mice, distinguishing them from the broader cohort.

In previous work, we have shown that aging in both *Ercc1*$^{\Delta/-}$ and wild-type mice is correlated with a gene-length-dependent transcriptional decline due to physical stalling of elongating RNA polymerases leading to a disbalance between long and short genes[4]. In the present study, we found a high similarity between transcriptional and translational profiles, suggesting that most of the gene-length-dependent transcriptional changes are likely "translated" to the protein level. Another feature, which is widely associated with aging but has remained largely elusive, is a progressive decoupling between the transcriptome and proteome[10,87,88]. At first sight this might seem difficult to rationalize with our observations; however, continuation of a gene-length-dependent disbalance onto the protein level might lead to incomplete multi-subunit protein complexes when one subunit derived from a larger gene is under-expressed due to the transcription mentioned above. Incomplete protein complexes can in turn trigger the unfolded protein response and induce degradation of the affected subunits[89,90] or trigger compensatory mechanisms[91]. Since cells contain numerous protein complexes, this might partially explain the disconnect between the transcriptome and proteome during aging. Future studies should investigate whether gene length–dependent transcriptional decline contributes to the loss of proteostasis during aging to evaluate the validity of this hypothesis. Moreover, the role of RNA damage-driven ribosome collision herein and its contribution to aging and related changes remains to be further investigated[92–94].

In conclusion, our data showed that DR in *Ercc1*$^{\Delta/-}$ mice elicited a multifaceted adaptive response, revealing alterations across several molecular pathways, including inflammation, protein synthesis, and cellular metabolism, while demonstrating the adaptive capacity of the translational machinery under conditions of stress and nutrient limitations. Moving forward, the influence of dietary composition, RNA homeostasis, and the proteome should be examined to shed further light on the interplay between genomic instability, metabolism, translational control, and lifespan.

Methods

Mouse models and ethics statement

Male *Ercc1*$^{\Delta/-}$ and wild-type (WT) littermate control *(Ercc1*$^{+/+}$*)* mice were obtained by crossing *Ercc1*$^{\Delta/+}$ (in a pure C57BL6J or FVB background) with *Ercc1*$^{+/-}$ mice (in a pure FVB or C57BL6J background, respectively) to yield *Ercc1*$^{\Delta/-}$ offspring with a genetically uniform F1 C57BL6J/FVB hybrid background. These two backgrounds were crossed to minimize unfavorable characteristics, like early onset of blindness in an FVB background or deafness in a C57BL6J background. Since *Ercc1*$^{\Delta/-}$ mice were

smaller, food was administered within the cages, and water bottles with long nozzles were used from around two weeks of age. Experiments were performed in accordance with the Principles of Laboratory Animal Care and with the guidelines approved by the Dutch Ethical Committee in full accordance with European legislation (DEC no. 139-12-13 and 139-12-18).

Housing conditions and dietary regimens

Animals were housed individually in ventilated cages under specific pathogen-free conditions, in carefully controlled environments (20–22 °C, 12h light:12h dark cycle). Mice were visually inspected daily and weighed weekly and scored blindly for gross morphological and motor abnormalities. All animals were bred and maintained on AIN93G synthetic pellets (Research Diet Services B.V., Wijk bij Duurstede, The Netherlands; gross energy content 4.9 kcal/g dry mass, digestible energy 3.97 kcal/g). On average, 6–16-week-old *Ercc1*$^{\Delta/-}$ mice ate 2.3 g of food per day. The animals that were given dietary restriction (DR) were so from 7 weeks of age, when development was largely completed, starting with 10% restriction. DR was gradually increased weekly by 10% until 30% DR (1.6 g/day), which was provided from 9 weeks of age onward as previously published[5]. Adult WT mice ate on average 3.0 g of food per day, resulting in 2.1 g/day for 30% DR and a reduction in body weight (**Fig. S1F**). To avoid alterations in the biological clock, food was provided to the animals just before the start of the dark (active) period, Zeitgeber Time (ZT) 12:00, except for the day of sacrifice, when no food was given prior to collect.

At 16 weeks of age, WT and *Ercc1*$^{\Delta/-}$ mice on AL and DR regimens were sacrificed at the beginning of the dark period between ZT13 and ZT16. In addition, a group of AL-fed 7-week-old *Ercc1*$^{\Delta/-}$ mice was included, representing a biologically younger age and as a control for the start of DR, and a group of AL-fed 104-week-old WT, for comparison to natural aging (**Fig. S1A**). Prior to weaning, animals were randomly divided over all groups to prevent selection bias. Animals were euthanized when necropsy age was reached, livers were snap frozen in liquid nitrogen, and stored at −80°C for molecular analysis.

mRNA sequencing

Snap-frozen liver specimens were lysed in QIAzol lysis reagent with the TissueLyser LT (QIAGEN), and RNA was isolated using the miRNeasy mini kit (QIAGEN; 217004) according to the manufacturer's protocol with optional on-column DNase I treatment (QIAGEN; 79254). RNA quality and quantity were assessed using the NanoDrop One (Thermo Fisher Scientific, USA) and Bioanalyzer 2100 (Agilent, Santa Clara, CA, USA; G2939BA), respectively. RNA integrity values ranged between 8.4 and 9.5. Samples were sent for mRNA paired-end 2*150 bp sequencing (Novogene, Cambridge, United Kingdom) on the Illumina NovaSeq6000 platform to a depth varying between 39887891 and 63618955 total reads per sample.

Ribosome profiling

Snap-frozen tissue samples from the same livers as used for mRNA sequencing were used to perform ribosome profiling with minimal modifications as previously described[95,96]. Samples were powdered with a BioSpec Pulverizer (#59012MS) on dry ice. Pulverized material was lysed with 500 µl ice-cold lysis buffer (20 mM Tris-Cl pH 7.4, 150 mM NaCl, 5 mM $MgCl_2$, 1% Triton X-100, 0.1% IGEPAL CA-630 (Sigma-Aldrich, USA), 1 mM DTT, 10 U/ml RNase-free DNase 1 (Lucigen, USA), 100 µg/ml cycloheximide (Sigma-Aldrich, USA)) for 15 minutes on ice, triturated ten times through a 23G needle, and clarified through centrifugation at 20000 g at 4 °C for 10 min. Total RNA content of sample lysates was estimated using the Qubit™ RNA broad range (BR) Assay Kit (Thermo Fisher Scientific, USA) on an Invitrogen™ Qubit™ 4 fluorometer (Thermo Fisher Scientific, USA). Lysates were then digested in 200 µl aliquots with RNAse I (10 units per 20 µg of RNA; Lucigen, USA) for generation of ribosome-protected fragments (RPFs) at 20 °C for 45 min while shaking at 400 RPM on a thermomixer. The digestion reaction was stopped by adding 5 µl (5U) of SUPERase*In RNAse inhibitor (Thermo Fisher Scientific, USA) and placing the samples on ice. Digested lysates were transferred to Microspin S-400 HR sephacryl columns (Sigma-Aldrich, USA) equilibrated with 3 ml of cold RNase-free polysome buffer (20 mM Tris-Cl pH 7.4, 150 mM NaCl, 5 mM $MgCl_2$) and centrifuged at 600 g at room temperature for 2 min. 10 µl of 10% SDS was added to the digested lysates, and RPFs were extracted using 3 volumes (660 µl) of Trizol LS (Fisher Scientific, USA), followed by the addition of 1 volume (880 µl) of ethanol and RNA purification using the Zymo Direct-zol RNA micro prep kit (Zymo Research, USA) with slight modifications to the manufacturer's instructions: Columns were spun dry for 1 min at 12000 g, and isolated RPFs were eluted in 20 µl nuclease-free water (Sigma-Aldrich, USA).

Depletion of rRNA was performed using RiboPOOL technology (siTOOLs Biotech; riboPOOL ribo-seq cat# dp-K012-000052, Germany) with a slight modification to the manufacturer's instructions: 200 pmol of RiboPOOL and 100 µl of beads were used per sample. Next, RNA was purified using the Zymo RNA Clean and Concentrator-5 kit (Zymo Research, USA) and size-selected through denaturing PAGE using 15% TBE-Urea gels (Thermo Fisher Scientific, USA). RNA fragments corresponding to 26–34 nucleotides were excised and recovered from gel slices by crushing the gel and rocking at 20 °C, 700 RPM for 2 hours on a thermomixer. RNA solutions were transferred to Costar Spin-X filter tubes (Thermo Fisher Scientific, USA) and filtered through centrifugation at 2350 g for 6 min. 2 µl of GlycoBlue (Thermo Fisher Scientific, USA) and 700 µl of isopropanol were added per aliquot, and RNA was left to precipitate overnight at −80 °C.

Following precipitation, RNA fragments were pelleted by centrifugation at 21130 g at 4 °C for 45 min. Pellets were washed with 1 ml of 80% ice-cold ethanol and centrifuged at 21130 g at 4 °C for 10 min. RNA pellets were air-dried for 3–4 min and dissolved in 60.75 µl nuclease-free water on ice. RNA fragments were dephosphorylated using 30 U of T4 PNK (Lucigen, USA) for 1 h at 37 °C and purified using the Zymo RNA Clean and Concentrator-5 kit (Zymo Research, USA), where isolated RNA fragments were eluted in 9.5 µl nuclease-free water. Purified fragments were ligated to a pre-adenylated 3' oligonucleotide linker using 100 U of T4 RNA ligase 2 Deletion Mutant (Lucigen, USA) and 5 U T4 RNA ligase 1 (Thermo Fisher Scientific, USA) at 23 °C for 3 h. Leftover linker was removed using 5' Deadenylase (New England Biolabs, USA) and Rec J Exonuclease (Lucigen, USA). Linker-ligated RNA fragments were reverse-transcribed into cDNA using EpiScript reverse transcriptase (Lucigen, USA). cDNA was treated with Exonuclease I (Lucigen, USA) for 30 min at 37 °C, followed by 15 min at 80 °C with a reduction to 4 °C, and further treated with 5 U of RNAse I (Lucigen, USA) and 2.5 U of Hybridase Thermostable RNase H (Lucigen, USA) at 55 °C for 5 min, followed by an incubation step at 4 °C to stop the reaction. Treated cDNA was purified using the Zymo Oligo

Clean and Concentrator Kit (Zymo Research, USA) with modifications to the manufacturer's instructions: Columns were spun dry for 1 min at 21130 g, and isolated RPFs were eluted in 9.5 µl nuclease-free water (Sigma-Aldrich, USA).

Size-selection of cDNA containing ligated linkers was performed through denaturing PAGE using 10% TBE-Urea gels (Thermo Fisher Scientific, USA). cDNA fragments corresponding to 70–80 nucleotides were excised and extracted with ammonium acetate and SDS, followed by overnight precipitation with isopropanol as described above. Size-selected cDNA was circularized for 3 h at 60 °C using 100 U of circLigase I (Lucigen, USA), followed by heat inactivation for 10 min at 80 °C, and amplified using Phusion high-fidelity polymerase (New England Biolabs, USA) with reverse primers containing unique barcode sequences for 10 cycles of 30 sec at 98 °C, 15 sec at 94 °C, 5 sec at 55 °C, and 10 sec at 65 °C. Following amplification, 5 µl of 3 M NaCl (Thermo Fisher Scientific, USA), 1 ml of ethanol, and 2 µl of GlycoBlue (Thermo Fisher Scientific, USA) were added to each aliquot of cDNA and left to precipitate overnight at −80 °C as described above.

Amplified cDNA libraries were size-selected using 8% non-denaturing TBE-Urea gels (Thermo Fisher Scientific, USA). cDNA libraries corresponding to 150 nucleotides were excised and recovered from gel slices by crushing and subsequent rocking at 37 °C at 700 RPM on a thermomixer for 2 hours. cDNA solutions were transferred to Costar Spin-X filter tubes (Thermo Fisher Scientific, USA) and filtered through centrifugation at 2350 g for 6 min. cDNA libraries were purified using the Zymo DNA Clean and Concentrator-5 kit (Zymo Research, USA) with modifications to the manufacturer's instructions: Columns were spun dry for 2 min at 12000 g and isolated RPFs were eluted in 13 µl nuclease-free water (Sigma-Aldrich, USA).

cDNA libraries were quantified using Qubit™ DNA high sensitivity (HS) Assay Kit (Thermo Fisher Scientific, USA) according to the manufacturer's instructions on an Invitrogen™ Qubit™ 4 fluorometer (Thermo Fisher Scientific, USA) and Bioanalyzer 2100 (Agilent) using the High Sensitivity DNA kit and pooled in equimolar ratios. Sequencing was performed on a NextSeq2000 (Illumina; 1×50 bp) at the Utrecht Sequencing Facility (USEQ) to a depth varying between 37831148 and 70879824 total reads per sample.

mRNA- and Ribo-seq data processing

Quality control of Ribo-seq data was performed by filtering reads for mitochondrial, rRNA, and tRNA sequence contaminations using Bowtie2 v2.4.2 (default settings, except; –seedlen 25)[97]. The resulting ribosome-protected fragments were consecutively aligned to the genome with STAR (version 2.7.3, default settings, except; sjdbOverhang 29, –outFilterMismatchNmax 2, –outSAMattributes = All, –outSAMtype SortedByCoordinate, –limitOutSJcollapsed 10000000, –limitIObufferSize 300000000, –alignSJoverhangMin 1000). RiboseQC v1.1[98] (default settings, except; read_subset = False, fast_mode = False) was used to check the quality of Ribo-seq samples and to extract footprint length distributions, periodicity (3 nt codon movement), and P-site counts from uniquely mapped reads. Quality control of mRNA data was performed with with FastQC v0.11.9.

For subsequent expression analysis, mRNA reads were treated as single-end and truncated to 28 nt to imitate ribosome-protected fragments. Next, both mRNA and ribo-seq datasets were treated identically, and processing of raw sequencing reads was performed on our in-house-generated data analysis pipeline. Removal of sequence adaptors, tRNA, and rRNA from both mRNA- and Ribo-seq and truncation of mRNA reads was performed using Trimmomatic (version 0.39). Trimmed reads were aligned to the coding region (CDS) of the mouse reference genome (annotation: gencode.vM20.annotation.gtf; genome: GRCm38.p6.genome.fa; http://gencodegenes.org/mouse/release_M20.html) using STAR (version 2.7.3). Read counts for each gene were obtained using FeatureCounts (as part of SubRead version 1.6.4), filtered using filterByExpr with count set to 10, followed by TMM normalization, quantification of log fold changes (logFC), and false discovery rates (FDR) using EdgeR (version 3.32.1). Statistically significant changes in mRNA- and ribo-seq data are referred to as differentially expressed genes (DEGs), depending on context.

For ORF quantification, ribosome-profiling adapters were clipped from reads and filtered for the standard quality threshold used by CutAdapt v3.4[99]. Fragments shorter than 25 nucleotides were discarded, and reads were filtered for contaminants using bowtie v2.4.2 as described above. The RPFs were mapped to the mouse genome (annotation: gencode.vM20.annotation.gtf; genome: GRCm38.p6.genome.fa; http://gencodegenes.org/mouse/release_M20.html) using STAR v2.7.8a and analyzed with ORFquant using default settings[100]. All CDS regions from the ORFquant output were analyzed for potential P-sites across all three frames by a custom Python script. In-frame P-sites were retained, yielding one nucleotide (NT) position per codon. An intersection operation was performed on the resulting BED file with the actual P-sites per sample calculated by ORFquant, providing the number of P-sites present per transcript per sample. Finally, logFC and FDR were calculated with EdgeR (version 3.32.1). Example images of canonical ORF and uORF translation were generated using the Integrative Genomics Viewer (IGV) by normalizing coverage data calculated by ORFquant[101].

Data analysis

Principal Component Analysis (PCA) was employed on the data normalized and mapped to coding sequences (CDS). We used the R Bioconductor packages "prcomp" and "gplots" for PCA analysis and plot generation, respectively. Enrichment analysis of pathways and upstream regulators was conducted using overrepresentation analysis (ORA). This process was facilitated through the Interactive Pathway Analysis (IPA) software (Ingenuity Systems, QIAGEN), designed to manage complex genomics data. For these analyses, we utilized a pre-filtered list of differentially expressed genes, selecting those with an FDR ≤ 0.05 and $\log(FC) > |0.5|$ to denote differential expression. Upstream regulator results were filtered to only include genes, RNAs, and proteins while excluding, for example, drug compounds, with Z-scores indicating the likely activation state of biological function. The identification of over-represented canonical pathways was achieved based on the data in the Ingenuity Pathways Knowledge Base. In IPA, gray bars represent pathways where activity predictions are not possible, while white bars indicate pathways with z-scores near zero or those ineligible for analysis due to fewer than four analysis-ready molecules (z-score = NaN).

GSEA (v4.3.2—build 13, standalone version) was run using TMM-normalized CPM values as input. For each comparison between groups (as shown in the figures), genes were ranked by signal-to-noise ratio, and enrichment scores were then calculated for predefined gene sets comprising annotated

mitochondrial and cytosolic ribosomal subunits and translation initiation factors (**Supplemental file 1**)[102]. Collapse/Remap to gene symbols was set to "No_collapse," and permutation type was set to "gene_set" to improve workflow for NGS data. All other settings were left at default.

Differential translational efficiency was examined using the DeltaTE software tool with standard settings and "batch" set to 0[103]. Genes were deemed differentially translated if they exhibited an FDR≤0.05. Pause site prediction and P-site codon occupancy were analyzed by the respective modules from Ribotoolkit using default settings[35]. Pause site prediction was powered by PausePred, which calculates the number of reads mapped to each position within a sliding window of length 1000 (step = length/2), considering footprints of 28–30 nt, normalizes these values over the average read density within the window, and computes the pause score as the average across overlapping windows[104]. For quantification of pause scores, those genes were used for which a pause score could be calculated in all genes using a default pause score threshold of 20 (n = 1228 genes). P-site codon occupancy was calculated with ribotoolkits and referenced as "absolute codon occupancy," as values are not automatically normalized for amino acid abundance. After normalization for differences in amino acid usage outside of ribotoolkits, the data was referenced as "relative codon occupancy." Heatmaps were based on edgeR normalized data and z-score transformed for visualization. Heatmaps based on ratio comparisons were log2 transformed before z-score transformation.

Statistics

Statistical analyses were performed using GraphPad Prism (GraphPad Software, La Jolla, CA, USA; version 9.2.0), DeltaTE[103], Ribotoolkit[35], IPA (Ingenuity Systems, QIAGEN), GSEA (v4.2.3 Build 10), or R Studio (2021.09.1, build 371). Significant p values were expressed as $*p \leq 0.05$, $**p \leq 0.01$, $***p \leq 0.001$, and $****p \leq 0.0001$. All data with error bars are presented as mean ± standard deviation (SD) as specified in figure legends. Nonparametric statistical analysis was applied to pause score analysis, as the data was not normally distributed. Statistical differences in pause score violin plots with two groups were calculated using the Mann–Whitney unpaired test in GraphPad Prism. Statistical differences in pause score violin plots comparing >2 groups were calculated using one-way ANOVA, and multiple comparisons testing was corrected for using Dunn's test, also in GraphPad Prism. Statistical significance and enrichment levels for the overlapping sections of the Venn diagrams were calculated using a custom R script based on hypergeometric distribution, as previously described[105]. Pie chart statistics were calculated based on cumulative binomial distribution probabilities.

Acknowledgments

We are grateful to Renata Brandt, Sander Barnhoorn, and the animal caretakers for general assistance with mouse experiments and Irene van Dijken and Willianne Vonk for experimental support. This research was funded by ONCODE, supported by the Dutch Cancer Society. J.H.J.H. was additionally supported by the National Institute of Health (NIH)/National Institute of Aging (NIA) (AG17242), the European Research Council Advanced Grant Dam2Age, and the Deutsche Forschungsgemeinschaft (DFG, German Research Foundation—Project-ID 73111208—SFB 829); J.H.J.H. and W.P.V. by Memorabel (ZonMW 733050810), BBoL (NWO-ENW 737.016.015), and the European Joint Programme Rare Diseases (TC-NER RD20-113); and W.P.V. by the Regiodeal Foodvalley (162135) and the ADPS Longevity Research Award.

Author Contributions

IvG, JHJH, and WPV conceptualized and designed the study. IvG, SAGE, and KS performed wet lab experiments. IvG, RAO, DAF, and JvD performed dry lab experiments and statistical analysis of data. IvG, SvH, JHJH, and WPV wrote this article, and RAO, DAF, JvD, SAGE, and KS contributed to editing this article. All authors contributed to the article and approved the submitted version.

Data Submission Statement

Raw data files for ribosome profiling and mRNA-seq have been submitted to the NCBI Gene Expression Omnibus (GEO) under accession numbers GSE288421 and GSE288427, respectively.

Conflicts of Interest

The authors declare that they have no actual or apparent conflict of interest between authorship of this study and any other activities.

AI Statement

Generative AI tools (ChatGPT4o/Claude 3.5 Sonnet) were used for minor improvements to grammar and sentence structure, but not for data acquisition or analysis. The authors reviewed and edited AI-generated changes and take full responsibility for the content of this publication.

Supplementary Materials

Supplemental information can be found here: Supplementary.

References

1. Schumacher, B., Pothof, J., Vijg, J., & Hoeijmakers, J.H.J. (2021). The central role of DNA damage in the ageing process. *Nature* **592**(7856), 695–703. PMID: 33911272; doi: 10.1038/s41586-021-03307-7.
2. Niedernhofer, L.J., Gurkar, A.U., Wang, Y., Vijg, J., Hoeijmakers, J.H.J., & Robbins, P.D. (2018). Nuclear genomic instability and aging. *Annu. Rev. Biochem.* **87**(1), 295–322. doi: 10.1146/annurev-biochem-062917-012239.
3. Vermeij, W.P., Hoeijmakers, J.H., & Pothof, J. (2014). Aging: not all DNA damage is equal. *Curr. Opin. Genet. Dev.* **26**, 124–130. PMID: 25222498; doi: 10.1016/j.gde.2014.06.006.
4. Gyenis, A., Chang, J., Demmers, J.J.P.G., Bruens, S.T., Barnhoorn, S., Brandt, R.M.C., … Pothof, J. (2023). Genome-wide RNA polymerase stalling shapes the transcriptome during aging. *Nat. Genet.* **55**(2), 268–279. PMID: 36658433; doi: 10.1038/s41588-022-01279-6.
5. Vermeij, W.P., Dollé, M.E.T., Reiling, E., Jaarsma, D., Payan-Gomez, C., Bombardieri, C.R., … Hoeijmakers, J.H.J. (2016). Restricted diet delays accelerated ageing and genomic stress in DNA-repair-deficient mice. *Nature.* **537**(7620), 427–431. PMID: 27556946; doi: 10.1038/nature19329.
6. Stoeger, T., Grant, R.A., McQuattie-Pimentel, A.C., Anekalla, K.R., Liu, S.S., Tejedor-Navarro, H., … Nunes Amaral, L.A. (2022). Aging is associated with a systemic length-associated transcriptome imbalance. *Nat. Aging* **2**(12), 1191–1206. PMID: 37118543; doi: 10.1038/s43587-022-00317-6.

7. Soheili-Nezhad, S., Ibáñez-Solé, O., Izeta, A., Hoeijmakers, J.H.J., & Stoeger, T. (2024). Time is ticking faster for long genes in aging. *Trends Genet.* S0168952524000271.
8. Walther, D.M., Kasturi, P., Zheng, M., Pinkert, S., Vecchi, G., Ciryam, P., … Hartl, F.U. (2015). Widespread Proteome Remodeling and Aggregation in Aging C. elegans. *Cell* **161**(4), 919–932. PMID: 25957690; doi: 10.1016/j.cell.2015.03.032.
9. Janssens, G.E., Meinema, A.C., González, J., Wolters, J.C., Schmidt, A., Guryev, V., … Heinemann, M. (2015). Protein biogenesis machinery is a driver of replicative aging in yeast. *eLife* **4**, e08527. doi: 10.7554/eLife.08527.
10. Kelmer Sacramento, E., Kirkpatrick, J.M., Mazzetto, M., Baumgart, M., Bartolome, A., Di Sanzo, S., … Ori, A. (2020). Reduced proteasome activity in the aging brain results in ribosome stoichiometry loss and aggregation. *Mol. Syst. Biol.* **16**(6), MSB209596. doi: 10.15252/msb.20209596.
11. Keele, G.R., Zhang, J.G., Szpyt, J., Korstanje, R., Gygi, S.P., Churchill, G.A., & Schweppe, D.K. (2023). Global and tissue-specific aging effects on murine proteomes. *Cell Rep.* **42**(7), 112715. PMID: 37405913; doi: 10.1016/j.celrep.2023.112715.
12. Anisimova, A.S., Alexandrov, A.I., Makarova, N.E., Gladyshev, V.N., & Dmitriev, S.E. (2018). Protein synthesis and quality control in aging. *Aging* **10**(12), 4269–4288. PMID: 30562164; doi: 10.18632/aging.101721.
13. Oh, H.S.H., Rutledge, J., Nachun, D., Pálovics, R., Abiose, O., Moran-Losada, P., … Wyss-Coray, T. (2023). Organ aging signatures in the plasma proteome track health and disease. *Nature* **624**(7990), 164–172. PMID: 38057571; doi: 10.1038/s41586-023-06802-1.
14. Loayza-Puch, F., Rooijers, K., Buil, L.C.M., Zijlstra, J., Oude Vrielink, J.F., Lopes, R., … Agami, R. (2016). Tumour-specific proline vulnerability uncovered by differential ribosome codon reading. *Nature* **530**(7591), 490–494. PMID: 26878238; doi: 10.1038/nature16982.
15. Hernández-Ortega, K., Garcia-Esparcia, P., Gil, L., Lucas, J.J., & Ferrer, I. (2016). Altered machinery of protein synthesis in Alzheimer's: From the nucleolus to the ribosome. *Brain Pathol.* **26**(5), 593–605. PMID: 26512942; doi: 10.1111/bpa.12335.
16. Anisimova, A.S., Meerson, M.B., Gerashchenko, M.V., Kulakovskiy, I.V., Dmitriev, S.E., & Gladyshev, V.N. (2020). Multifaceted deregulation of gene expression and protein synthesis with age. *Proc. Natl. Acad. Sci.* **117**(27), 15581–15590. PMID: 32576685; doi: 10.1073/pnas.2001788117.
17. Stein, K.C., Morales-Polanco, F., van der Lienden, J., Rainbolt, T.K., & Frydman, J. (2022). Ageing exacerbates ribosome pausing to disrupt cotranslational proteostasis. *Nature* **601**(7894), 637–642. PMID: 35046576; doi: 10.1038/s41586-021-04295-4.
18. Woodward, K. & Shirokikh, N.E. (2021). Translational control in cell ageing: an update. *Biochem. Soc. Trans.* **49**(6), 2853–2869. PMID: 34913471; doi: 10.1042/BST20210844.
19. Di Fraia, D., Marino, A., Lee, J.H., Kelmer Sacramento, E., Baumgart, M., Bagnoli, S., … Ori, A. (2025). Altered translation elongation contributes to key hallmarks of aging in the killifish brain. *Science* **389**(6759): eadk3079. PMID: 40743332; doi: 10.1126/science.adk3079.
20. Li, G.H., Zhu, X.Q., Xiao, F.H., Zhao, X., Lv, L., Yin, F.Q., … Kong, Q.P. (2025). A multi-omics molecular landscape of 30 tissues in aging female rhesus macaques. *Nat. Methods* **22**(12), 2658–2669. PMID: 41249656; doi: 10.1038/s41592-025-02912-y.
21. Kathjoo, M.B. & Srivastava, M. (2022 June) A link between DNA double-strand breaks and regulation of global translation. *FEBS J.* **289**(11), 3093–3096. doi: 10.1111/febs.16398.
22. Boon, N.J., Oliveira, R.A., Körner, P.R., Kochavi, A., Mertens, S., Malka, Y., … Brummelkamp, T.R. (2024). DNA damage induces p53-independent apoptosis through ribosome stalling. *Science* **384**(6697), 785–792. PMID: 38753784; doi: 10.1126/science.adh7950.
23. Bournique, E., Sanchez, A., Oh, S., Ghazarian, D., Mahieu, A.L., Manjunath, L., … Buisson R. (2025 Apr). ATM and IRAK1 orchestrate two distinct mechanisms of NF-κB activation in response to DNA damage. *Nat. Struct. Mol. Biol.* **32**(4), 740–755. doi: 10.1038/s41594-024-01417-0.
24. Vermeij, W.P., Hoeijmakers, J.H.J., & Pothof, J. (2016). Genome integrity in aging: Human syndromes, mouse models, and therapeutic options. *Annu. Rev. Pharmacol. Toxicol.* **56**(1), 427–445. doi: 10.1146/annurev-pharmtox-010814-124316.
25. Perez, K., Parras, A., Picó, S., Rechsteiner, C., Haghani, A., Brooke, R., … Ocampo, A. (2024). DNA repair-deficient premature aging models display accelerated epigenetic age. *Aging Cell.* **23**(2), e14058. PMID: 38140713; doi: 10.1111/acel.14058.
26. Weeda, G., Donker, I., De Wit, J., Morreau, H., Janssens, R., Vissers, C.J., … Hoeijmakers, J.H.J. (1997). Disruption of mouse ERCC1 results in a novel repair syndrome with growth failure, nuclear abnormalities and senescence. *Curr. Biol.* **7**(6), 427–439. PMID: 9197240; doi: 10.1016/S0960-9822(06)00190-4.
27. Dollé, M.E.T., Kuiper, R.V., Roodbergen, M., Robinson, J., de Vlugt, S., Wijnhoven, S.W.P., … van Steeg, H. (2011). Broad segmental progeroid changes in short-lived *Ercc1* $^{-/\Delta 7}$ mice. *Pathobiol Aging Age-Relat Dis.* **1**(1), 7219.
28. White, R.R., Milholland, B., MacRae, S.L., Lin, M., Zheng, D., & Vijg, J. (2015). Comprehensive transcriptional landscape of aging mouse liver. *BMC Genomics*. **16**(1), 899. doi: 10.1186/s12864-015-2061-8.
29. Gregg, S.Q., Gutiérrez, V., Rasile Robinson, A., Woodell, T., Nakao, A., Ross, M.A., … Niedernhofer, L.J. (2012). A mouse model of accelerated liver aging caused by a defect in DNA repair. *Hepatology* **55**(2), 609–621. PMID: 21953681; doi: 10.1002/hep.24713.
30. Chen, L., Ma, M.Y., Sun, M., Jiang, L.Y., Zhao, X.T., Fang, X.X., … Song, B.L. (2019). Endogenous sterol intermediates of the mevalonate pathway regulate HMGCR degradation and SREBP-2 processing. *J. Lipid Res.* **60**(10), 1765–1775. PMID: 31455613; doi: 10.1194/jlr.RA119000201.
31. Klaassen, C.D. & Aleksunes, L.M. (2010). Xenobiotic, bile acid, and cholesterol transporters: function and regulation. *Pharmacol. Rev.* **62**(1), 1–96. PMID: 20103563; doi: 10.1124/pr.109.002014.
32. Ponsuksili, S., Murani, E., Brand, B., Schwerin, M., & Wimmers, K. (2011). Integrating expression profiling and whole-genome association for dissection of fat traits in a porcine model. *J. Lipid Res.* **52**(4), 668–678. PMID: 21289033; doi: 10.1194/jlr.M013342.
33. Zhao, Y., Simon, M., Seluanov, A., & Gorbunova, V. (2023). DNA damage and repair in age-related inflammation. *Nat. Rev. Immunol.* **23**(2), 75–89. PMID: 35831609; doi: 10.1038/s41577-022-00751-y.
34. Gulhar, R., Ashraf, M.A., & Jialal, I. (2023). Physiology, acute phase reactants. StatPearls [Internet]. Treasure Island (FL): StatPearls Publishing. Retrieved from: http://www.ncbi.nlm.nih.gov/books/NBK519570/ (accessed on 9 January 2024).
35. Liu, Q., Shvarts, T., Sliz, P., & Gregory, R.I. (2020). RiboToolkit: an integrated platform for analysis and annotation of ribosome profiling data to decode mRNA translation at codon resolution. *Nucleic Acids Res.* **48**(W1), W218–W229. PMID: 32427338; doi: 10.1093/nar/gkaa395.
36. Khitun, A., Ness, T.J., & Slavoff, S.A. (2019). Small open reading frames and cellular stress responses. *Mol Omics*. **15**(2), 108–116. PMID: 30810554; doi: 10.1039/C8MO00283E.
37. Young, S.K. & Wek, R.C. (2016). Upstream open reading frames differentially regulate gene-specific translation in the integrated stress response. *J. Biol. Chem.* **291**(33), 16927–16935. PMID: 27358398; doi: 10.1074/jbc.R116.733899.
38. Barbosa, C., Peixeiro, I., & Romão, L. (2013). Gene expression regulation by upstream open reading frames and human disease. Fisher EMC, editor. *PLoS Genet.* **9**(8), e1003529. doi: 10.1371/journal.pgen.1003529.
39. Chen, H.H. & Tarn, W.Y. (2019). uORF-mediated translational control: recently elucidated mechanisms and implications in cancer. *RNA Biol.* **16**(10), 1327–1338. PMID: 31234713; doi: 10.1080/15476286.2019.1632634.
40. Silva, J., Fernandes, R., & Romão, L. (2019). Translational regulation by upstream open reading frames and human diseases. In: Romão L., ed. *The mRNA Metabolism in Human Disease.*, 99–116. Cham: Springer International Publishing. doi: 10.1007/978-3-030-19966-1_5.

41. Johnstone, T.G., Bazzini, A.A., & Giraldez, A.J. (2016). Upstream ORF s are prevalent translational repressors in vertebrates. *EMBO J*. **35**(7), 706–723. PMID: 26896445; doi: 10.15252/embj.201592759.

42. Sung, B., Park, S., Yu, B.P., & Chung, H.Y. (2004). Modulation of PPAR in aging, inflammation, and calorie restriction. *J. Gerontol. A Biol. Sci. Med. Sci.* **59**(10), B997–B1006. doi: 10.1093/gerona/59.10.B997.

43. Nevedomskaya, E., Meissner, A., Goraler, S., De Waard, M., Ridwan, Y., Zondag, G., … Mayboroda, O.A. (2010). Metabolic profiling of accelerated aging ERCC1$^{d/-}$ mice. *J. Proteome Res.* **9**(7), 3680–3687. PMID: 20507129; doi: 10.1021/pr100210k.

44. Czerwińska, J., Nowak, M., Wojtczak, P., Dziuban-Lech, D., Cieśla, J.M., Kołata, D., … Tudek, B. (2018). ERCC1-deficient cells and mice are hypersensitive to lipid peroxidation. *Free Radic Biol. Med*. **124**, 79–96. PMID: 29860127; doi: 10.1016/j.freeradbiomed.2018.05.088.

45. Huang, J., Tabbi-Anneni, I., Gunda, V., & Wang, L. (2010). Transcription factor Nrf2 regulates SHP and lipogenic gene expression in hepatic lipid metabolism. *Am. J. Physiol. Gastrointest Liver Physiol*. **299**(6), G1211–G1221. PMID: 20930048; doi: 10.1152/ajpgi.00322.2010.

46. Im, S.S., Yousef, L., Blaschitz, C., Liu, J.Z., Edwards, R.A., Young, S.G., … Osborne, T.F. (2011). Linking lipid metabolism to the innate immune response in macrophages through sterol regulatory element binding protein-1a. *Cell Metab* **13**(5), 540–549. PMID: 21531336; doi: 10.1016/j.cmet.2011.04.001.

47. Schumacher, B., van der Pluijm, I., Moorhouse, M.J., Kosteas, T., Robinson, A.R., Suh, Y., … Garinis, G.A. (2008). Delayed and accelerated aging share common longevity assurance mechanisms. *PLoS Genet. United States* **4**(8), e1000161.

48. Wilson, K.A., Chamoli, M., Hilsabeck, T.A., Pandey, M., Bansal, S., Chawla, G., & Kapahi P. (2021). Evaluating the beneficial effects of dietary restrictions: A framework for precision nutrigeroscience. *Cell Metab*. **33**(11), 2142–2173. PMID: 34555343; doi: 10.1016/j.cmet.2021.08.018.

49. Rasa, S.M.M., Annunziata, F., Krepelova, A., Nunna, S., Omrani, O., Gebert, N., … Neri, F. (2022). Inflammaging is driven by upregulation of innate immune receptors and systemic interferon signaling and is ameliorated by dietary restriction. *Cell Rep*. **39**(13), 111017.

50. Yang, H., Zingaro, V.A., Lincoff, J., Tom, H., Oikawa, S., Oses-Prieto, J.A., … Ruggero, D. (2024). Remodelling of the translatome controls diet and its impact on tumorigenesis. *Nature* **633**(8028), 189–197. doi: 10.1038/s41586-024-07781-7.

51. Todisco, S., Santarsiero, A., Convertini, P., De Stefano, G., Gilio, M., Iacobazzi, V., & Infantino, V. (2022). PPAR alpha as a metabolic modulator of the liver: role in the pathogenesis of nonalcoholic steatohepatitis (NASH). *Biology* **11**(5), 792. PMID: 35625520; doi: 10.3390/biology11050792.

52. He, Y., Yang, W., Huang, L., Mever, M.A., Ramautar, R., Harms, A., … Hankemeier, T. (2024). Metabolomic analysis of dietary-restriction-induced attenuation of sarcopenia in prematurely aging DNA repair-deficient mice. *J. Cachexia Sarcopenia Muscle* **15**(3), 868–882. PMID: 38689513; doi: 10.1002/jcsm.13433.

53. Xu, A.F., Molinuevo, R., Fazzari, E., Tom, H., Zhang, Z., Menendez, J., … Barna, M. (2023). Subfunctionalized expression drives evolutionary retention of ribosomal protein paralogs Rps27 and Rps27l in vertebrates. *eLife* **12**, e78695. PMID: 37306301; doi: 10.7554/eLife.78695.

54. Lopes, I., Altab, G., Raina, P., & De Magalhães, J.P. (2021). Gene size matters: an analysis of gene length in the human genome. *Front Genet.* **12**, 559998. PMID: 33643374; doi: 10.3389/fgene.2021.559998.

55. Ibañez-Solé, O., Barrio, I., & Izeta, A. (2023). Age or lifestyle-induced accumulation of genotoxicity is associated with a length-dependent decrease in gene expression. *iScience* **26**(4), 106368. PMID: 37013186; doi: 10.1016/j.isci.2023.106368.

56. Moshage, H. (1997). Cytokines and the hepatic acute phase response. *J. Pathol*. **181**(3), 257–266. PMID: 9155709; doi: 10.1002/(SICI)1096-9896(199703)181:3<257::AID-PATH756>3.0.CO;2-U.

57. Porukala, M. & Vinod, P.K. (2023). Network-level analysis of ageing and its relationship with diseases and tissue regeneration in the mouse liver. *Sci. Rep*. **13**(1), 4632.

58. Cohen, I., Rider, P., Vornov, E., Tomas, M., Tudor, C., Wegner, M., … Schneider, R. (2015). IL-1α is a DNA damage sensor linking genotoxic stress signaling to sterile inflammation and innate immunity. *Sci. Rep*. **5**(1), 14756.

59. Härtlova, A., Erttmann, S.F., Raffi, F.A.m., Schmalz, A.M., Resch, U., Anugula, S., … Gekara, N.O. (2015). DNA damage primes the type I interferon system via the cytosolic DNA sensor STING to promote anti-microbial innate immunity. *Immunity* **42**(2), 332–343. PMID: 25692705; doi: 10.1016/j.immuni.2015.01.012.

60. Gulen, M.F., Samson, N., Keller, A., Schwabenland, M., Liu, C., Glück, S., … Ablasser, A. (2023). cGAS–STING drives ageing-related inflammation and neurodegeneration. *Nature* **620**(7973), 374–380. PMID: 37532932; doi: 10.1038/s41586-023-06373-1.

61. Bock, K.W. (2019). Functions of aryl hydrocarbon receptor (AHR) and CD38 in NAD metabolism and nonalcoholic steatohepatitis (NASH). *Biochem. Pharmacol.* **169**, 113620. PMID: 31465774; doi: 10.1016/j.bcp.2019.08.022.

62. Bock, K.W. (2021). Aryl hydrocarbon receptor (AHR) functions in infectious and sterile inflammation and NAD+-dependent metabolic adaptation. *Arch Toxicol.* **95**(11), 3449–3458. PMID: 34559251; doi: 10.1007/s00204-021-03134-9.

63. Birkisdóttir, M.B., van Galen, I., Brandt, R.M.C., Barnhoorn, S., van Vliet, N., van Dijk, C., … Vermeij, W.P. (2022). The use of progeroid DNA repair-deficient mice for assessing anti-aging compounds, illustrating the benefits of nicotinamide riboside. *Front Aging. Switzerland* **3**, 1005322. doi: 10.3389/fragi.2022.1005322.

64. Hou, Y., Lautrup, S., Cordonnier, S., Wang, Y., Croteau, D.L., Zavala, E., … Bohr, V.A. (2018). NAD(+) supplementation normalizes key Alzheimer's features and DNA damage responses in a new AD mouse model with introduced DNA repair deficiency. *Proc. Natl. Acad Sci. USA. United States* **115**(8), E1876–E1885.

65. Scheibye-Knudsen, M., Mitchell, S.J., Fang, E.F., Iyama, T., Ward, T., Wang, J., … Bohr, V.A. (2014). A high-fat diet and NAD(+) activate Sirt1 to rescue premature aging in cockayne syndrome. *Cell Metab. United States* **20**(5), 840–855. doi: 10.1016/j.cmet.2014.10.005.

66. Kane, A., Chellappa, K., Schultz, M., Diener, C., Gibbons, S., Baur, J., … Sinclair, D. (2023). Long-term nmn treatment increases lifespan and healthspan in mice in a sex dependent manner. *Innov. Aging* **7** (Supplement_1), 1077–1077. doi: 10.1093/geroni/igad104.3459.

67. Fang, E.F., Hou, Y., Lautrup, S., Jensen, M.B., Yang, B., SenGupta, T., … Bohr, V.A. (2019). NAD+ augmentation restores mitophagy and limits accelerated aging in Werner syndrome. *Nat. Commun.* **10**(1), 5284. PMID: 31754102; doi: 10.1038/s41467-019-13172-8.

68. Wek, R.C. (2018). Role of eIF2α Kinases in Translational Control and Adaptation to Cellular Stress. *Cold Spring Harb Perspect Biol.* **10**(7), a032870. PMID: 29440070; doi: 10.1101/cshperspect.a032870.

69. Dennis, M.D., Jefferson, L.S., & Kimball, S.R. (2012). Role of p70S6K1-mediated phosphorylation of eIF4B and PDCD4 proteins in the regulation of protein synthesis. *J. Biol. Chem*. **287**(51), 42890–42899. PMID: 23105104; doi: 10.1074/jbc.M112.404822.

70. Zhang, D., Zhou, Y., Ma, Y., Jiang, P., Lv, H., Liu, S., … Jin, Y. (2022). Ribosomal protein L22-like1 (RPL22L1) mediates sorafenib sensitivity via ERK in hepatocellular carcinoma. *Cell Death Discov*. **8**(1), 365. PMID: 35973992; doi: 10.1038/s41420-022-01153-8.

71. Zhang, Y., O'Leary, M.N., Peri, S., Wang, M., Zha, J., Melov, S., … Wiest, D.L. (2017). Ribosomal proteins Rpl22 and Rpl22l1 control morphogenesis by regulating pre-mRNA splicing. *Cell Rep*. **18**(2), 545–556.

72. Wu, N., Wei, J., Wang, Y., Yan, J., Qin, Y., Tong, D., … Jin, Y. (2015). Ribosomal L22-like1 (RPL22L1) promotes ovarian cancer metastasis by inducing epithelial-to-mesenchymal transition. Guan XY, editor. *PLOS ONE*. **10**(11), e0143659.

73. Xiong, X., Zhao, Y., Tang, F., Wei, D., Thomas, D., Wang, X., … Sun, Y. (2014). Ribosomal protein S27-like is a physiological regulator of p53 that suppresses genomic instability and tumorigenesis. *eLife* **3**, e02236. doi: 10.7554/eLife.02236.

74. Xiong, X., Liu, X., Li, H., He, H., Sun, Y., & Zhao, Y. (2018). Ribosomal protein S27-like regulates autophagy via the β-TrCP-DEPTOR-mTORC1

axis. *Cell Death Dis*. **9**(11), 1131. PMID: 30425236; doi: 10.1038/s41419-018-1168-7.

75. Hountondji, C., Bulygin, K., Créchet, J.B., Woisard, A., Tuffery, P., Nakayama, J., … Baouz, S. (2014). The CCA-end of P-tRNA contacts both the human RPL36AL and the A-site bound translation termination factor eRF1 at the peptidyl transferase center of the human 80S ribosome. *Open Biochem. J*. **8**(1), 52–67. doi: 10.2174/1874091X01408010052.
76. Barger, J.L., Anderson, R.M., Newton, M.A., Da Silva, C., Vann, J.A., Pugh, T.D., … Weindruch, R. (2015). A conserved transcriptional signature of delayed aging and reduced disease vulnerability is partially mediated by SIRT3. Vina J, editor. *PLOS ONE*. **10**(4), e0120738. doi: 10.1371/journal.pone.0120738.
77. Gonskikh, Y. & Polacek, N. (2017). Alterations of the translation apparatus during aging and stress response. *Mech. Ageing Dev*. **168**, 30–36. PMID: 28414025; doi: 10.1016/j.mad.2017.04.003.
78. Di Fraia, D., Marino, A., Lee, J.H., Kelmer Sacramento, E., Baumgart, M., Bagnoli, S., … Ori A. (2024). Impaired biogenesis of basic proteins impacts multiple hallmarks of the aging brain [Preprint]. *bioRxiv*. doi: 10.1101/2023.07.20.549210.
79. Folgueras, A.R., Freitas-Rodríguez, S., Velasco, G., & López-Otín, C. (2018). Mouse models to disentangle the hallmarks of human aging. *Circ. Res*. **123**(7), 905–924. PMID: 30355076; doi: 10.1161/CIRCRESAHA.118.312204.
80. Godet, A.C., David, F., Hantelys, F., Tatin, F., Lacazette, E., Garmy-Susini, B., & Prats, A.C. (2019). IRES Trans-Acting Factors, Key Actors of the Stress Response. *Int. J. Mol. Sci*. **20**(4), 924. PMID: 30791615; doi: 10.3390/ijms20040924.
81. Santinha, D., Vilaça, A., Estronca, L., Schüler, S.C., Bartoli, C., De Sandre-Giovannoli, A., … Ferreira, L. (2024). Remodeling of the cardiac extracellular matrix proteome during chronological and pathological aging. *Mol. Cell Proteomics* **23**(1), 100706. PMID: 38141925; doi: 10.1016/j.mcpro.2023.100706.
82. Niedernhofer, L.J., Garinis, G.A., Raams, A., Lalai, A.S., Robinson, A.R., Appeldoorn, E., … Hoeijmakers, J.H.J. (2006). A new progeroid syndrome reveals that genotoxic stress suppresses the somatotroph axis. *Nature. England* **444**(7122), 1038–1043. doi: 10.1038/nature05456.
83. Van Der Linden, J., Stefens, S.J.M., Heredia-Genestar, J.M., Ridwan, Y., Brandt, R.M.C., Van Vliet, N., … Van Der Pluijm, I. (2024). Ercc1 DNA repair deficiency results in vascular aging characterized by VSMC phenotype switching, ECM remodeling, and an increased stress response. *Aging Cell* **23**(5), e14126. doi: 10.1111/acel.14126.
84. Paine, P.T., Rechsteiner, C., Morandini, F., Desdín-Micó, G., Mrabti, C., Parras, A., … Ocampo, A. (2024). Initiation phase cellular reprogramming ameliorates DNA damage in the ERCC1 mouse model of premature aging. *Front. Aging* **4**, 1323194. PMID: 38322248; doi: 10.3389/fragi.2023.1323194.
85. Perez, K., Parras, A., Picó, S., Rechsteiner, C., Haghani, A., Brooke, R., … Ocampo, A. (2024). DNA repair-deficient premature aging models display accelerated epigenetic age. *Aging Cell* **23**(2), e14058. doi: 10.1111/acel.14058.
86. Vanhooren, V., Dewaele, S., Libert, C., Engelborghs, S., De Deyn, P.P., Toussaint, O., … Chen, C.C. (2010). Serum N-glycan profile shift during human ageing. *Exp. Gerontol*. **45**(10), 738–743. PMID: 20801208; doi: 10.1016/j.exger.2010.08.009.
87. Wei, Y.N., Hu, H.Y., Xie, G.C., Fu, N., Ning, Z.B., Zeng, R., & Khaitovich, P. (2015). Transcript and protein expression decoupling reveals RNA binding proteins and miRNAs as potential modulators of human aging. *Genome Biol*. **16**(1), 41. PMID: 25853883; doi: 10.1186/s13059-015-0608-2.
88. Khatir, I., Brunet, M.A., Meller, A., Amiot, F., Patel, T., Lapointe, X., … Laurent, B. (2023). Decoupling of mRNA and protein expression in aging brains reveals the age-dependent adaptation of specific gene subsets. *Cells* **12**(4), 615. PMID: 36831282; doi: 10.3390/cells12040615.
89. Ishikawa K. (2021). Multilayered regulation of proteome stoichiometry. *Curr. Genet*. **67**(6), 883–890. PMID: 34382105; doi: 10.1007/s00294-021-01205-z.
90. Mueller, S., Wahlander, A., Selevsek, N., Otto, C., Ngwa, E.M., Poljak, K., … Gauss, R. (2015). Protein degradation corrects for imbalanced subunit stoichiometry in OST complex assembly. Gilmore R, editor. *Mol. Biol. Cell*. **26**(14), 2596–2608. PMID: 25995378; doi: 10.1091/mbc.E15-03-0168.
91. Kovács, D., Biró, J.B., Ahmed, S., Kovács, M., Sigmond, T., Hotzi, B., … Barna, J. (2024). Age-dependent heat shock hormesis to HSF -1 deficiency suggests a compensatory mechanism mediated by the unfolded protein response and innate immunity in young Caenorhabditis elegans. *Aging Cell* **23**(10), e14246. doi: 10.1111/acel.14246.
92. Cordes, J., Zhao, S., Engel, C.M., & Stingele, J. (2025). Cellular responses to RNA damage. *Cell* **188**(4), 885–900. PMID: 39983673; doi: 10.1016/j.cell.2025.01.005.
93. Zaher, H.S. & Mosammaparast, N. (2025) RNA damage responses in cellular homeostasis, genome stability, and disease. *Annu. Rev. Pathol. Mech. Dis*. **20**(1), 433–457. doi: 10.1146/annurev-pathmechdis-111523-023516.
94. Tsao, N., Lombardi, P.M., Park, A., Olabode, J., Rodell, R., Sun, H., … Mosammaparast, N. (2025). YTHDC1 cooperates with the THO complex to prevent RNA-damage-induced DNA breaks. *Mol. Cell* **85**(6), 1085–1100.e9. PMID: 40037355; doi: 10.1016/j.molcel.2025.02.003.
95. McGlincy, N.J. & Ingolia, N.T. (2017). Transcriptome-wide measurement of translation by ribosome profiling. *Methods San Diego Calif*. **126**, 112–129. PMID: 28579404; doi: 10.1016/j.ymeth.2017.05.028.
96. Palomar-Siles, M., Heldin, A., Zhang, M., Strandgren, C., Yurevych, V., Van Dinter, J.T., … Wiman, K.G. (2022). Translational readthrough of nonsense mutant TP53 by mRNA incorporation of 5-Fluorouridine. *Cell Death Dis*. **13**(11), 997. PMID: 36433934; doi: 10.1038/s41419-022-05431-2.
97. Langmead, B. & Salzberg, S.L. (2012) Fast gapped-read alignment with Bowtie 2. *Nat. Methods* **9**(4), 357–359. PMID: 22388286; doi: 10.1038/nmeth.1923.
98. Calviello, L., Sydow, D., Harnett, D., & Ohler, U. (2019). Ribo-seQC: comprehensive analysis of cytoplasmic and organellar ribosome profiling data [Preprint]. *bioRxiv*. doi: https://doi.org/10.1101/601468.
99. Martin, M. (2011). Cutadapt removes adapter sequences from high-throughput sequencing reads. *EMBnet. J*. **17**(1), 10. doi: 10.14806/ej.17.1.200.
100. Calviello, L., Hirsekorn, A., & Ohler, U. (2020). Quantification of translation uncovers the functions of the alternative transcriptome. *Nat. Struct. Mol. Biol*. **27**(8), 717–725. PMID: 32601440; doi: 10.1038/s41594-020-0450-4.
101. Robinson, J.T., Thorvaldsdóttir, H., Winckler, W., Guttman, M., Lander, E.S., Getz, G., & Mesirov, J.P. (2011). Integrative genomics viewer. *Nat. Biotechnol*. **29**(1), 24–26. PMID: 21221095; doi: 10.1038/nbt.1754.
102. Subramanian, A., Tamayo, P., Mootha, V.K., Mukherjee, S., Ebert, B.L., Gillette, M.A., … Mesirov, J.P. (2005). Gene set enrichment analysis: A knowledge-based approach for interpreting genome-wide expression profiles. *Proc. Natl. Acad. Sci*. **102**(43), 15545–15550. PMID: 16199517; doi: 10.1073/pnas.0506580102.
103. Chothani, S., Adami, E., Ouyang, J.F., Viswanathan, S., Hubner, N., Cook, S.A., … Rackham, O.J.L. (2019). deltaTE: Detection of translationally regulated genes by integrative analysis of Ribo-seq and RNA-seq data. *Curr. Protoc. Mol. Biol*. **129**, e108. doi: 10.1002/cpmb.108.
104. Kumari, R., Michel, A.M., & Baranov, P.V. (2018). PausePred and Rfeet: webtools for inferring ribosome pauses and visualizing footprint density from ribosome profiling data. *RNA*. **24**(10), 1297–1304. PMID: 30049792; doi: 10.1261/rna.065235.117.
105. Zhou, Q., Chipperfield, H., Melton, D.A., & Wong, W.H. (2007). A gene regulatory network in mouse embryonic stem cells. *Proc. Natl. Acad. Sci*. **104**(42), 16438–16443. PMID: 17940043; doi: 10.1073/pnas.0701014104.